

# Validation of E-region Model Electron Density Profiles with AURIC utilizing High-Resolution Cross Sections

Md Nazmus Sakib<sup>1</sup>, Emmaris Soto<sup>2</sup>, Erdal Yiğit<sup>3</sup>, J Scott Evans<sup>2</sup>, and R R Meier<sup>3</sup>

<sup>1</sup>Affiliation not available

<sup>2</sup>Computational Physics Inc

<sup>3</sup>Department of Physics and Astronomy, Space Weather Lab, George Mason University

September 11, 2023

## Abstract

E-region models have traditionally underestimated the ionospheric electron density. We believe that this deficiency can be remedied by using high-resolution photoabsorption and photoionization cross sections in the models. Deep dips in the cross sections allow solar radiation to penetrate deeper into the E-region producing additional ionization. To validate our concept, we perform a study of model electron density profiles (EDPs) calculated using the Atmospheric Ultraviolet Radiance Integrated Code (AURIC; `\citeA{strickland1999atmospheric}`) in the E-region of the terrestrial ionosphere. We compare AURIC model outputs using new high-resolution photoionization and photoabsorption cross sections, and solar spectral irradiances during low solar activity with incoherent scatter radar (ISR) measurements from the Arecibo and Millstone Hills observatories, COSMIC-1 observations, and outputs from empirical models (IRI-2016 and FIRI-2018). AURIC results utilizing the new high-resolution cross sections reveal a significant difference to model outputs calculated with the low-resolution cross sections currently used. Analysis of AURIC EDPs using the new high-resolution data indicate fair agreement with ISR measurements obtained at various times at Arecibo but very good agreement with Millstone Hills ISR observations from  $\sim 96$  km to  $140$  km. However, discrepancies in the altitude of the E-region peak persist. High-resolution AURIC calculations are in agreement with COSMIC-1 observations and IRI-2016 model outputs between  $\sim 105$  km and  $140$  km while FIRI-2018 outputs underestimate the EDP in this region. Overall, AURIC modeling shows increased E-region electron densities when utilizing high-resolution cross sections and high-resolution solar irradiances, and are likely to be the key to resolving the long standing data-model discrepancies.

# Validation of E-region Model Electron Density Profiles with AURIC utilizing High-Resolution Cross Sections

MD Nazmus Sakib<sup>1</sup>, Emmaris Soto<sup>2</sup>, Erdal Yiğit<sup>1</sup>, J. Scott Evans<sup>2</sup>, R. R Meier<sup>1</sup>

<sup>1</sup>Department of Physics and Astronomy, Space Weather Lab, George Mason University, Fairfax, VA 22030, USA

<sup>2</sup>Computational Physics Inc., 8001 Braddock Rd, Suite 210, Springfield, VA 22151, USA

## Key Points:

- AURIC simulations are updated utilizing high-resolution photoionization and photoabsorption cross sections and scaled solar spectra.
- Multi instrument observations have been used to compare electron density profiles with AURIC E-region high-resolution modeling efforts.
- New high-resolution calculations show improvement in the E-region electron density calculation by producing more ionization.

---

Corresponding author: Md Nazmus Sakib, msakib@gmu.edu

## Abstract

E-region models have traditionally underestimated the ionospheric electron density. We believe that this deficiency can be remedied by using high-resolution photoabsorption and photoionization cross sections in the models. Deep dips in the cross sections allow solar radiation to penetrate deeper into the E-region producing additional ionization. To validate our concept, we perform a study of model electron density profiles (EDPs) calculated using the Atmospheric Ultraviolet Radiance Integrated Code (AURIC; D. Strickland et al. (1999)) in the E-region of the terrestrial ionosphere. We compare AURIC model outputs using new high-resolution photoionization and photoabsorption cross sections, and solar spectral irradiances during low solar activity with incoherent scatter radar (ISR) measurements from the Arecibo and Millstone Hills observatories, COSMIC-1 observations, and outputs from empirical models (IRI-2016 and FIRI-2018). AURIC results utilizing the new high-resolution cross sections reveal a significant difference to model outputs calculated with the low-resolution cross sections currently used. Analysis of AURIC EDPs using the new high-resolution data indicate fair agreement with ISR measurements obtained at various times at Arecibo but very good agreement with Millstone Hills ISR observations from  $\sim 96$  km to 140 km. However, discrepancies in the altitude of the E-region peak persist. High-resolution AURIC calculations are in agreement with COSMIC-1 observations and IRI-2016 model outputs between  $\sim 105$  km and 140 km while FIRI-2018 outputs underestimate the EDP in this region. Overall, AURIC modeling shows increased E-region electron densities when utilizing high-resolution cross sections and high-resolution solar irradiances, and are likely to be the key to resolving the long standing data-model discrepancies.

## 1 Introduction

The E-region ionosphere is a natural plasma laboratory where neutral processes play an important role in shaping the ionosphere. While photochemical processes are crucial in establishing the structure of the E-region (Chu et al., 2009), dynamical processes, such as tidal and gravity wave propagation, and dissipation modulate the underlying neutral structures (Yigit & Medvedev, 2015). These processes form the terrestrial ionosphere that extends from  $\sim 60$  km up to  $\sim 1000$  km above the surface of the Earth and contains multiple distinct regions of charged particles (D, E, and F regions), characterized by the variation of the electron density as a function of height. Each of these layers has its own density maximum at a certain height.

43 Although the ionospheric E-region was the first to be discovered (E. V. Appleton & Bar-  
44 nett, 1925), the details of the physical and chemical processes governing the mean and variable  
45 structure of this region are still not well understood. Thus, validation of E-region electron den-  
46 sity modeling and better characterization of the altitude variations of plasma density in this re-  
47 gion is extremely important. One complexity of the E-region ionosphere, which coincides in al-  
48 titude with the lower thermosphere, is that it is influenced by processes from below and above  
49 (Yigit et al., 2016; Ward et al., 2021; Shiokawa & Georgieva, 2021). Various photochemical pro-  
50 cesses are predominant in the E-region and it is often challenging to decouple the sources of vari-  
51 ability in observations. Therefore, idealized numerical models, such as the Atmospheric Ultra-  
52 violet Radiance Integrated Code (AURIC; D. Strickland et al. (1999)), are a powerful tool to iso-  
53 late sources of variability.

54 The primary objective of this paper is to validate the latest version of AURIC, by compar-  
55 ing E-region model electron density profiles (EDPs) with observations from both ground-based  
56 (e.g., radars) and space-borne instruments (e.g., satellites) along with other existing empirical mod-  
57 els, and to study the E-region ionospheric structure and variability. Previously, D. Strickland et  
58 al. (1999) compared the initial version of AURIC with a number of observations by rockets and  
59 satellite measurements in terms of photoelectron flux, dayglow and ion density distribution mea-  
60 sured by AE-E satellite photoelectron flux data, FUV and MUV dayglow rocket data, AE-E ion-  
61 mass spectrometry data, respectively. These studies showed reasonable agreement between the  
62 data and model. For the first time, in this study, we utilize EDPs as a probe to compare outputs  
63 from high resolution AURIC calculations with state-of-the-art ground-based and space-borne ob-  
64 servations.

## 65 **2 Brief Description of the Instruments and Models**

### 66 **2.1 Instrument Description**

#### 67 **2.1.1 Arecibo ISR**

68 The Arecibo incoherent scatter radar (ISR) is situated at Arecibo, Puerto Rico (18.44°N,  
69 293.2°E) and is very well known in the field of ionospheric and astrophysics research. In this study,  
70 we particularly selected data described in the work by Sojka et al. (2014), which is a radar cam-  
71 paign to understand the low latitude E-region EDPs on February 9, 2012. The local time at Arecibo  
72 is given in ‘Atlantic Standard Time’ (AST), which is 4 hours behind of Universal Time Coordi-  
73 nate (UTC) i.e.,  $UTC = AST + 4$ .

### 2.1.2 *Millstone Hills ISR*

The ISR at Millstone Hills (42.61°N, 288.5°E) is another well known ground based radar which is used in observing mid latitude ionospheric EDPs (e.g., Lei et al., 2005; Zhang et al., 2011; Yan et al., 2020, and references therein). Millstone Hills ISR observes ionospheric EDPs using two different techniques: alternating code (AC) and single pulse (SP). While SP provides data at a vertical resolution of about 18 km, AC provides data at a resolution of about 4.5 km. Our study utilizing AC data contains electron density information below 400 km (Lei et al., 2007). We downloaded data from the MIT Madrigal Database for February 16, 2012, which has similar geomagnetic and solar condition in comparison with Arecibo ISR campaign data on February 9, 2012 (see section 3 for more detail).

### 2.1.3 *COSMIC-1 GPS Radio Occultation (RO)*

The Constellation Observing System for Meteorology Ionosphere and Climate, also called COSMIC-1 (USA) or Formosa Satellite Mission-3 - FORMOSAT-3 (Taiwan) (Anthes et al., 2008), consists of 6 small equidistant satellites forming a constellation in a circular orbit at around 800 km from the surface of the Earth (Chu et al., 2009). This system of satellites was successfully launched on April 15, 2006 and retired in 2020. The University Corporation for Atmospheric Research - COSMIC Data Analysis and Archive Center (UCAR-CDAAC) provides COSMIC-1 level 2 ionospheric profile data, reprocessed in 2013 and 2021. Based on an inversion technique to get electron density profiles from radio signal refractivity, there are two kinds of COSMIC-1 radio occultation profiles, namely “ion-profile” and “iga-profile”. Ion profiles data are the refracted signals of occultations measurements inverted using the standard Abel inversion method which assumes spherical symmetry. The latter one is recently updated, removing the spherical symmetry assumption, and considering the horizontal gradient of atmospheric constituents. All of these profiles can be used for various scientific purposes, but our study will use more improved iga profiles as these profiles are expected to produce less error in E-region electron density measurement. Any typical ion profile or iga profile contains vertical electron density, total vertical electron content, mean sea level altitude of observed profiles ( $\sim 50$  km to  $\sim 800$  km), occultation azimuth angle and perigee point geolocations (i.e., latitude and longitude) of the observation (top to bottom).

McGranaghan et al. (2015) compared a set of COSMIC-1 RO data with an improved version of GLOW (an ionospheric numerical model) (Solomon et al., 1988; Bailey et al., 2002) which

105 calculates electron transport and chemical reactions with optimized time (GLOWfast) along with  
106 the older version (GLOWfull) in terms of electron number density vertical profiles and found rea-  
107 sonable agreement at the bottom side of the E-region, though their analysis also showed discrep-  
108 ancy (less than factor of two) in upper E-region. None of the COSMIC-1 and GLOW model com-  
109 parisons produce agreement in terms of E-region peak height (shifted by  $\sim 5$  to  $\sim 10$  km).

110 Prior to that, Sheng et al. (2014) compared COSMIC electron density profiles with ground  
111 based ISR focusing on the F-region and found profiles during summer time are more reliable though  
112 the electron density profiles extend down to around 100 km.

113 The systematic and observational error of radio occultations by COSMIC satellites is well  
114 explained in Lei et al. (2007). That paper compared COSMIC individual electron density ver-  
115 tical profiles with Millstone Hills and Jicamarca radar observations in similar geolocations. For  
116 the topside ionosphere, COSMIC data is more suitable to study as horizontal gradient has min-  
117 imum effect on EDPs (Lai et al., 2013). However, this study will use COSMIC-1 EDPs (iga for-  
118 mat) at E-region which is more improved and considers horizontal gradient effects (Pedatella et  
119 al., 2015) to compare with our model AURIC.

## 120 **2.2 Model Description**

### 121 **2.2.1 AURIC**

122 AURIC is an integrated physics-based model developed by Computational Physics Inc. to  
123 calculate the the upper atmospheric spectral radiance (airglow) from the FUV to near infrared,  
124 including aerosol and Rayleigh scattering of sunlight and moonlight from the middle and lower  
125 atmosphere, and densities of species that are chemically active above 100 km from the surface  
126 of the Earth (D. Strickland et al., 1999). The term ‘integrated’ refers to the combination of a UV  
127 radiance model with Air Force model MODTRAN (Berk et al., 1987). Details about the devel-  
128 opment of AURIC can be found in previous works by Link et al. (1993); D. J. Strickland et al.  
129 (1996); Majeed and Strickland (1997, and references there in). AURIC requires direct user in-  
130 puts including date and universal coordinate time (UTC), geographic latitude and longitude, ob-  
131 server altitude and look angle and spectral interval and resolution. Derived user inputs are ge-  
132 omagnetic latitude and longitude, dip angle, solar zenith angle, solar local time (LST), F10.7 (cur-  
133 rent and 81-day average) and AP history. The first version of AURIC used generated file inputs  
134 such as model neutral atmosphere by Mass Spectrometer and Incoherent Scatter data thermosphere  
135 model (MSIS-E-90) (Hedin, 1991) and SHARC and MODTRAN Merged (SAMM) (Sharma et

136 al., 1996) of  $N_2$ ,  $O_2$ ,  $O$ ,  $N$ ,  $NO$ ,  $O_3$  species, model ionosphere by Fully Analytic Ionospheric Model  
 137 (FAIM; Anderson et al., 1989), geomagnetic field by corrected geomagnetic coordinates (GEO-  
 138 CGM; Gustafsson et al., 1992), and incident solar EUV spectrum by Hinteregger et al. (1981).  
 139 In that version, database files and encoded data inputs are photoabsorption and photoionization  
 140 cross sections (Conway, 1988; Bell & Stafford, 1992), solar reference EUV spectrum (Hinteregger  
 141 et al., 1981), electron impact cross sections, chemical rate coefficients, molecular transition ar-  
 142 rays, and molecular population distributions. For convenience, we refer to the low-resolution AU-  
 143 RIC cross sections as “Conway”, even though his is a compilation from many sources. The Con-  
 144 way report can be accessed at Conway (1988). The current version of AURIC has been modi-  
 145 fied with a new high-resolution calculation of photoionization and photoabsorption cross sections  
 146 for  $O$  updated from Meier et al. (2007) and  $N_2$  (Soto et al., 2023) along with new high-resolution  
 147 calculations of solar spectral irradiance (Warren, 2005). **Our primary interest is to determine**  
 148 **and report if model calculations using new high resolution solar spectral irradiances and**  
 149 **photoionization and photoabsorption cross sections resolve prior data-model discrepancies**  
 150 **with E-region EDPs.**

### 151 2.2.2 IRI-2016

152 The International Reference Ionosphere (IRI) is an empirical model widely used for iono-  
 153 spheric reference initiated jointly by the Committee on Space Research (COSPAR) and the In-  
 154 ternational Union of Radio Science (URSI) since the late sixties for the most important plasma  
 155 parameters in Earth’s ionosphere (Bilitza et al., 1993). An updated review of the model can be  
 156 found in the work by Bilitza et al. (2022). The first widely circulated edition was IRI-78 (Rawer  
 157 et al., 1978); however, our study utilizes the latest version IRI-2016 (Bilitza et al., 2017). This  
 158 new version of IRI takes additional input of peak electron density ( $N_m F2$ ) at F2 height ( $h_m F2$ ),  
 159 and an improved description of ion composition at high and low solar activity based on data from  
 160 satellites such as C/NOFS-CINDI. Other input parameters of this model are solar indices F10.7  
 161 radio flux (daily, 81-days, and 12-months running mean), sunspot number  $R_z$  (13-months run-  
 162 ning mean), Ionospheric index such as ionosonde-based  $IG$  index (12-months running mean) (Brown  
 163 et al., 2018) and geomagnetic index such as  $A_p$  index (daily average, 3-hour planetary). The web-  
 164 based version of this model can predict altitude profiles of electron density, electron temperature,  
 165 ion temperature, major ion composition and total electron content (TEC) from 50 km to 2000 km  
 166 for those specific inputs.

### 167 2.2.3 *FIRI-2018*

168 Our study utilizes another empirical model at lower altitudes in the ionosphere called Faraday-  
 169 International Reference Ionosphere (FIRI)-2018 (Friedrich et al., 2018) originally published in  
 170 2001 as a semi-empirical model (Friedrich & Torkar, 2001). This is a specialized IRI model for  
 171 the non-auroral ionosphere valid for altitudes above 60 km up to 150 km. One can utilize the python  
 172 based version of this model varying four input parameters such as day (Julian day of the year from  
 173 1-365), solar zenith angle (0-130°), latitude (0-60°) and solar radio flux F10.7 (75-200 solar flux  
 174 unit).

## 175 3 Geomagnetic conditions on the observational days

176 Figure 1 shows a time plot of geomagnetic and solar EUV activity for February (29 days)  
 177 in 2012. The vertical solid and dotted red lines in Figure 1 identify February 9 and February 16,  
 178 respectively, which correspond to the data analyzed here. For first four panels, we utilize data pro-  
 179 vided by the Adolf-Schmidt-Observatory for Geomagnetism in Niemegk operated by the GFZ  
 180 German Research Center for Geosciences (Matzka et al., 2021). The top two panels (a and b) show  
 181 the planetary Kp index (three-hourly equivalent) at 12:00-15:00 UT and daily equivalent plan-  
 182 etary Ap index, which is the arithmetic mean of three-hour equivalent Ap values of the whole day  
 183 calculated from Kp. History and a detailed description of these geomagnetic indices can also be  
 184 found in Bartels (1949, 1957); Matzka et al. (2021, and references therein). Local noon time ob-  
 185 served 10.7 cm solar radio flux ( $F_{10.7}$ ) is presented in Figure 1(c) in the unit of s.f.u. ( $= 10^{-22}$   
 186  $\text{W m}^{-2} \text{Hz}^{-1}$ ), using a dataset provided by the Dominion Radio Astrophysical Observatory and  
 187 National Research Council, Canada (Tapping, 2013). Figure 1(d) shows the individual interna-  
 188 tional sunspot number (SN) provided by the Royal Observatory of Belgium in Brussels. Descrip-  
 189 tions of the SN series based on all the corrections by different observations are given in the work  
 190 by Clette and Lefèvre (2016). Data source for GOES X-ray (Figure 1(e)) is NOAA Space Weather  
 191 Prediction Center (SWPC) and we have utilized GOES-15 level 2 X-ray sensor 1-minute irra-  
 192 diance average for the entire month of February 2012. On the other hand, source of hourly equa-  
 193 torial Dst index data (Figure 1(f)) is World Data Center for Geomagnetism, Kyoto, Japan.

## 194 4 Analysis and Results

195 In this study, we investigate the impact on E-region electron densities of new photoioniza-  
 196 tion and photoabsorption “high-resolution” cross sections used in the AURIC model (Soto et al.,  
 197 2023), along with model output using the “low-resolution” cross sections from Conway (1988).

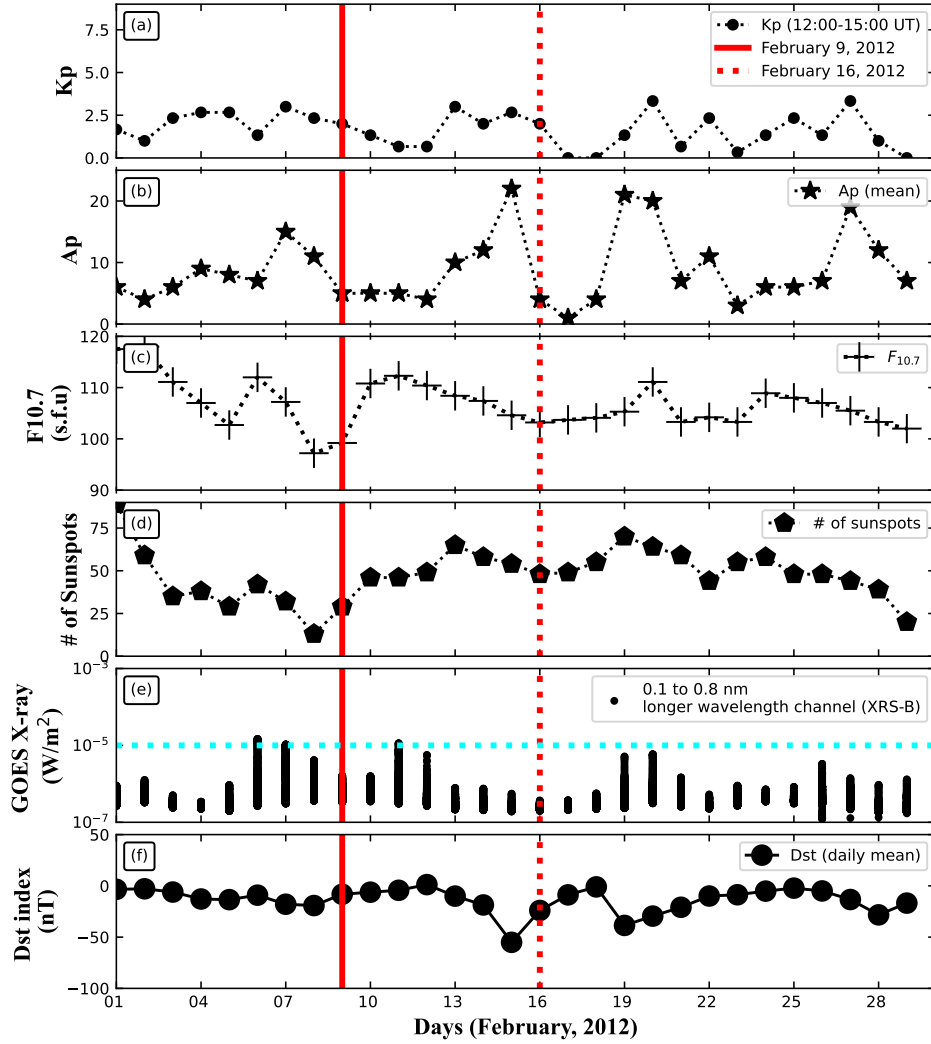


**Figure 1.** Geomagnetic index and solar condition for the month of February 2012 (29 days). Panel a and b : Kp (dot symbol) and Ap (star symbol) index. Panel c and d : F10.7 (plus symbol) and sunspot number (pentagon symbol). Panel e: GOES-15 level 2 X-ray sensor 1-minute irradiance daily average. Cyan horizontal line indicates the lower limit of solar M-class flare. Panel f: Disturbance storm time (Dst) index. February 9, 2012 is represented by the vertical red solid line and February 16, 2012 by the vertical red dotted line.

198 We carry out model simulations by AURIC for February 9 and 16, 2012, which are consistent  
 199 with observational data by Arecibo and Millstone Hills ISRs. In a companion paper, Soto et al.  
 200 (2023) describe the details of the new high-resolution cross sections and solar spectral irradiance.  
 201 That paper shows that the implementation of new high-resolution inputs in the model increases  
 202 the total photoionization rate (133%) in the E-region. Using the same high-resolution photoion-  
 203 ization and photoabsorption cross sections and solar spectral irradiances, we validate AURIC model  
 204 outputs with state-of-the-art remote sensing observations.

#### 205 **4.1 Comparison between AURIC and Arecibo ISR**

206 Figure 2 shows three different “hourly” mean EDPs and corresponding individual EDPs  
 207 observed by Arecibo ISR on 9 February 2012 during daytime conditions. The whole data set con-  
 208 sists of 82 EDPs from 8:03 Hr AST to 16:00 Hr AST from 90 km to  $\sim 400$  km.

209 The morning profile represents Arecibo observations at 8-9 Hr AST or 12-13 Hr UTC. Sim-  
 210 ilarly, the noon profile (12-13 AST) corresponds to 16-17 Hr UTC and afternoon profile (15-16  
 211 AST) corresponds to 19-20 Hr UTC. These hourly binned mean EDPs show local solar time vari-  
 212 ation with maximum ionization at noon in terms of peak electron density at the E-region ( $N_m E$ ).  
 213 The shaded region around hourly mean EDPs in Figure 2 represent the  $1-\sigma$  standard deviation  
 214 of measurements at each altitude step. As expected theoretically, the maximum ionization oc-  
 215 curs around local noon. Additionally, hourly mean EDPs remain almost invariant from 90 km  
 216 to 95 km (at  $\sim 96$  km, the noon mean EDP shows a 36% discrepancy with the morning mean  
 217 EDP and 31% discrepancy with the afternoon mean EDP) and more distinctive above  $\sim 100$  km  
 218 (at  $\sim 102$  km, the noon mean EDP shows a 74% discrepancy with the morning mean EDP and  
 219 12% discrepancy with the afternoon mean EDP).

220 Arecibo observations show peak E-region EDP heights ( $h_m E$ ) at  $\sim 114$  km for morning,  
 221  $\sim 108$  km for noon, and  $\sim 106$  km for afternoon times. At these altitudes, the mean  $N_m E$  val-  
 222 ues are  $\sim 9.29 \pm 1.01 \times 10^{10} \text{ m}^{-3}$ ,  $\sim 1.53 \pm 0.02 \times 10^{11} \text{ m}^{-3}$  and  $\sim 1.21 \pm 0.09 \times 10^{11}$   
 223  $\text{m}^{-3}$ , respectively.

224 To compare these real time Arecibo observations with AURIC calculated electron density  
 225 profiles, we assumed electrical quasi-neutrality, i.e., the number density of positive ions is equal  
 226 to the number density of electrons, or  $n_e = \sum_i n_i$ , where  $i$  represents the number of positive  
 227 ion species (Prölss, 2012). We summed up five major ‘long lived’ positive ions including  $\text{NO}^+$ ,  
 228  $\text{O}_2^+$ ,  $\text{O}^+$ ,  $\text{N}^+$ , and  $\text{N}_2^+$  to construct the electron density altitude profiles.

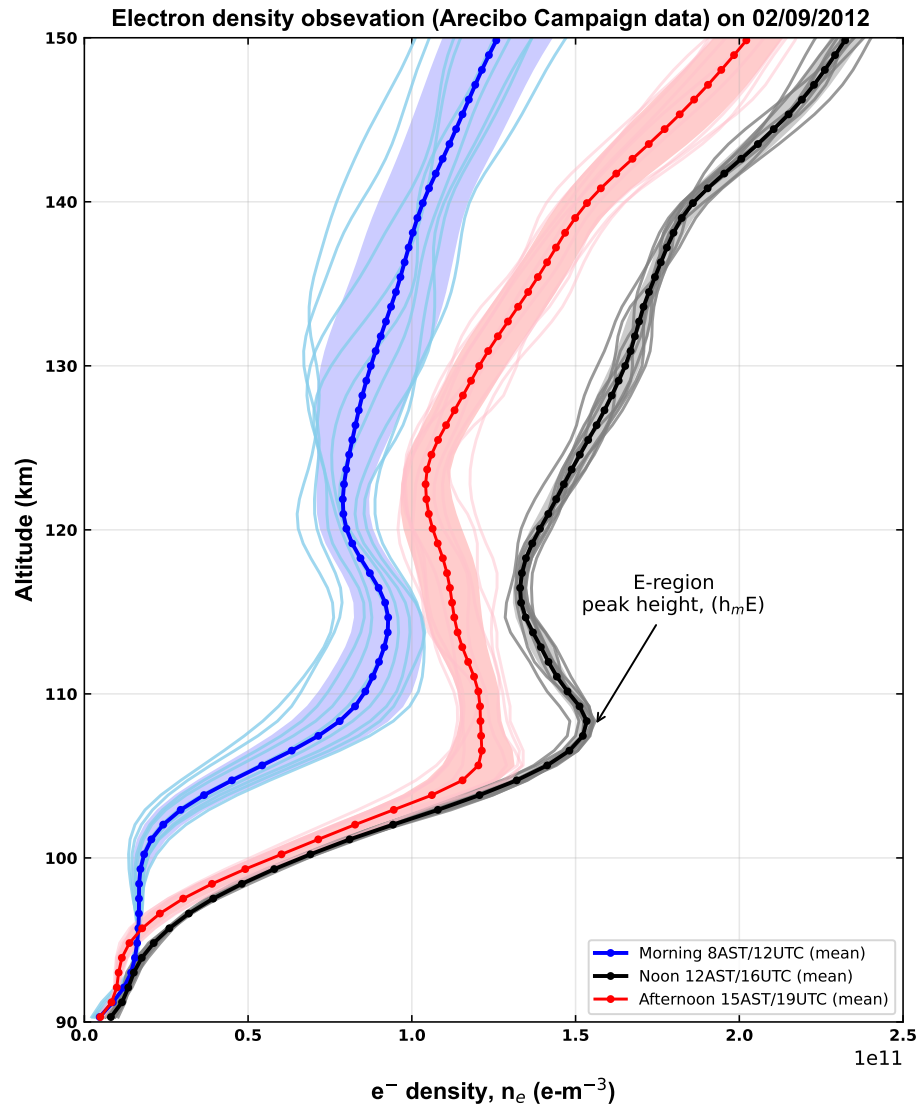


**Figure 2.** Arecibo ISR measured sunlit atmosphere hourly mean electron density as a function of altitude at 8:00 (blue), 12:00 (black) and 15:00 (red) AST observed by Arecibo ISR (18.44°N, -66.67°W) on February 9, 2012. Light blue, grey and pink profiles represent the raw observations within those hours. Shaded region in each profile shows 1- $\sigma$  standard deviation that represents natural variability of the data.

229 As mentioned earlier, to understand the impact of high-resolution cross sections and so-  
 230 lar spectral irradiances in model simulations, we used both the low-resolution cross sections from  
 231 the Conway (1988) compilation and the newly calculated high-resolution cross sections as in-  
 232 puts to the model. Additionally, this study utilizes a new high-resolution solar EUV spectrum con-  
 233 structed by scaling the high-resolution spectrum data delivered by H. Warren and Sherry Chhabra  
 234 for Feb 9 and Feb 16, 2012. We put the solar spectrum on an absolute irradiance scale using a  
 235 model of the solar EUV spectral irradiance (Lean et al., 2011) updated with the latest data (Lean  
 236 et al., 2020; Woods et al., 2012; Lean et al., 2003) to compute solar spectral irradiance (see com-  
 237 panion paper by Soto et al., 2023).

238 Two different AURIC runs can be seen in each panel of Figure 3. Curves labeled ‘low-resolution’  
 239 refer to model simulations based on low-resolution Conway cross sections with a low-resolution  
 240 solar spectrum and ‘high-resolution’ refers to model results using high-resolution cross section  
 241 data with high-resolution solar spectrum. The high-resolution cross sections have a resolution  
 242 of 0.001 nm while the low-resolution cross sections have a resolution of 0.05 nm below 10 nm  
 243 and 0.1 nm above 10 nm. The original resolution of the delivered solar spectrum is 0.001 nm;  
 244 however, in order to run AURIC for the low-resolution case we bin the high-resolution spectrum  
 245 onto the low-resolution AURIC grid (see Soto et al., 2023, for more detail).

246 Non-auroral E-region electron density profile can be characterized by a modest peak ( $N_m E$ )  
 247 located near  $\sim 105\text{--}110$  km, which is a function of solar radiation, atmospheric composition,  
 248 and atmospheric temperature (Solomon, 2006). Our work partially focuses on a comparison study  
 249 of peak values of EDPs and heights of the peak EDPs ( $h_m E$ ) between data and model to gain  
 250 insight about data-model discrepancies given the high uncertainty of the peak values and heights.  
 251 A derivative parameter, the E-region critical frequency ( $f_o E$ ), is directly proportional to peak elec-  
 252 tron density ( $N_m E$ ), and is also a conventional measure in the ionospheric physics community  
 253 (see Appendix B for more detail). Our comparison is conducted by calculating the relative per-  
 254 cent differences of these values between data and model. A quantitative comparison between Arecibo  
 255 observations and AURIC runs is shown in Table 1 where the relative percentage difference (de-  
 256 noted by  $\Delta_{rel}(\%)$ ) of AURIC calculations with respect to Arecibo observations is calculated by,

$$257 \quad \Delta_{rel} = \frac{|AURIC - Arecibo|}{Arecibo} * 100\% \quad (1)$$

258 Specifically, during morning and in terms of  $N_m E$ , the mean absolute difference between  
 259 the low-resolution AURIC ion production rate and the Arecibo ISR data is  $\sim 32\%$  whereas the

260 mean absolute difference for the high-resolution model output is  $\sim 33\%$ , as can be seen from  
 261 from Figure 3(a) and Table 1(a). Clearly, the AURIC morning time high-resolution EDP is shifted  
 262 towards real time observation than the low-resolution AURIC run. However, the high resolution  
 263 cross sections do not preserve the characteristic E-region local maxima in between  $\sim 105$  km  
 264 and  $\sim 110$  km during a sunlit condition, in contrast with low-resolution AURIC runs. There-  
 265 fore, we used the observed  $h_m E$  to estimate the AURIC  $N_m E$  for comparison with the observed  
 266  $N_m E$ . Tables 1(b) and 1(c) likewise show values of  $N_m E$ ,  $h_m E$ ,  $f_o E$ , and the corresponding  
 267 discrepancy between data and model for noon and afternoon times, respectively.

268 During noon time (see Figure 3(b)), the Arecibo observed  $N_m E$  ( $f_o E$ ) shows  $\sim 13(\sim 7)\%$   
 269 and  $\sim 18(\sim 9)\%$  discrepancy with respect to the high-resolution and low-resolution model cal-  
 270 culations. At afternoon time (see Figure 3(c)), Arecibo ISR observation and AURIC model dis-  
 271 crepancy is  $\sim 4(2)\%$  and  $\sim 6(3)\%$ , for high and low-resolution runs, respectively.

272 The low-resolution AURIC results agree better with data during the afternoon time (see  
 273 Figure 3(c)). In order to investigate the reason for this, we checked multiple factors, such as the  
 274 impact of changing the photoionization and photoabsorption cross section magnitude, difference  
 275 of photoabsorption cross section, volume production rate, and the neutral atmospheric input in  
 276 the model. We reached the conclusion that the E-region electron density peak can be better re-  
 277 produced provided that  $O_2$  high resolution cross sections are implemented as well. Figure S1 in  
 278 the Supporting Information illustrates the strong dependence of the lower EDP peak with the  $O_2^+$   
 279 (X) ionization rate as a function of altitude, and to a lesser extent the dependence on the  $O^+$  ( $^4S_o$ )  
 280 ionization rate. The large contributions from these states, particularly the  $O_2^+$  (X) state, between  
 281 approximately 105-130 km reflect an increase in the transmission dictated by the structure in the  
 282 high-resolution  $N_2$  photoabsorption cross section. Incorporation of high-resolution  $O_2$  photoab-  
 283 sorption and photoionization cross sections may further impact the ionization rate magnitude and  
 284 peak, and thus shape of the EDP. Additionally, several other missing physical processes in the  
 285 model, such as lack of diffusion mechanism, atmospheric extinction at E-layer specially absorp-  
 286 tion of solar X-rays and EUV at this altitude, and as a consequence secondary ionization by en-  
 287 ergetic photoelectrons, or other dynamical processes, such as ion drifts and ion-neutral interac-  
 288 tions could produce the similarity with the low-resolution results. Using high-resolution physics  
 289 in the model could potentially reveal or highlight the importance of the above mentioned pro-  
 290 cesses that are currently not accounted for. Overall, the high-resolution AURIC output produces  
 291 more ionization at E-region than the previously employed low-resolution cross sections of AU-  
 292 RIC runs.

**Arecibo ISR and AURIC  
electron density profiles comparison  
Morning, Noon, Afternoon - 02/09/2012**

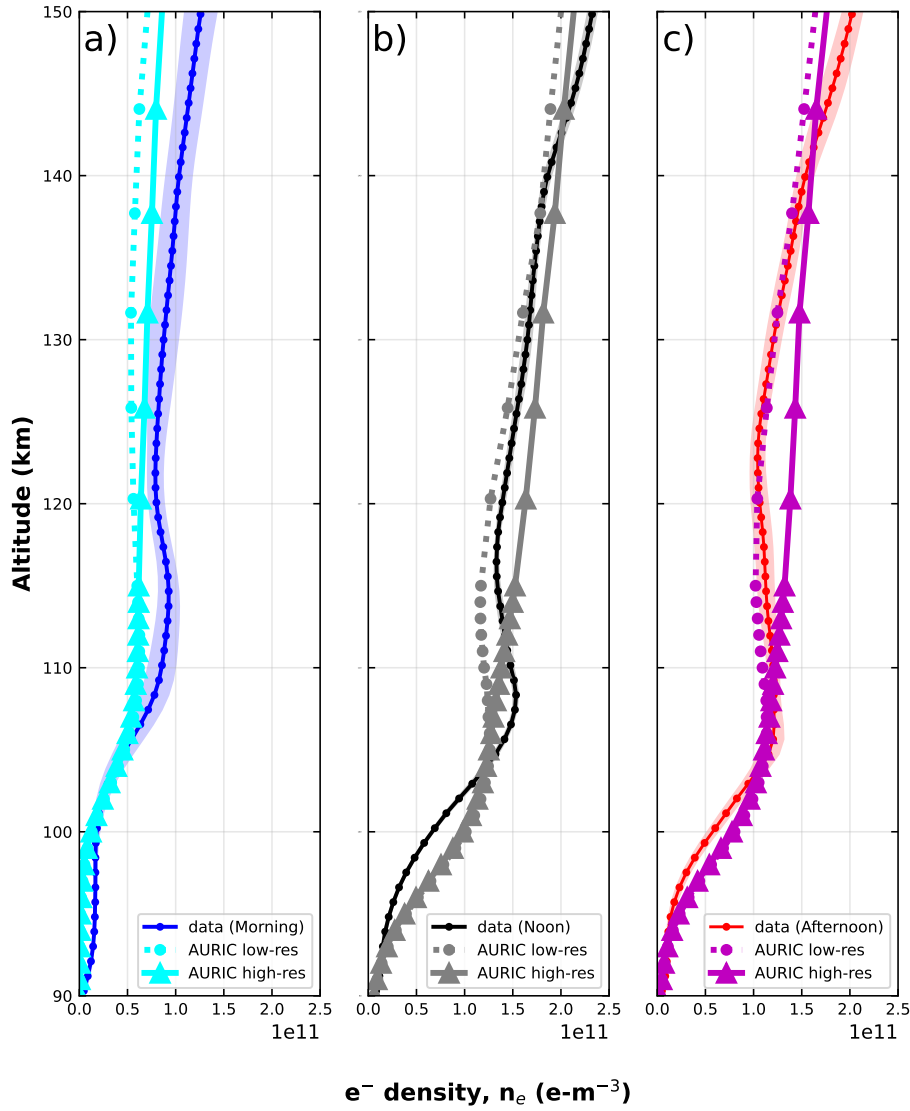


**Figure 3.** Daytime electron density comparison between data and model. Electron density as a function of altitude calculated by AURIC at a) (right panel) 8 AST/12 UTC (cyan), b) (middle panel) 12 AST/16 UTC (grey) and c) (left panel) 15 AST/19 UTC (magenta) with two different sets of cross section - low-resolution (circular dashed line) and high-resolution (triangular solid line) overlapped with Arecibo ISR measured EDPs ( $e^- m^{-3}$ ) at the same time. Blue, black, and red profiles represents Arecibo ISR observations at local solar time morning, noon, and afternoon, respectively on that day (same as Figure 2). See text for more detail.

**Table 1.** Quantitative Comparison between Arecibo ISR observation and AURIC

Morning <sup>a</sup>	$N_m E$ ( $e^-/m^3$ )	$h_m E$ ( $km$ )	$f_o E$ ( $MHz$ )	$\Delta_{rel}(N_m E)$ (%)	$\Delta_{rel}(h_m E)$ (%)	$\Delta_{rel}(f_o E)$ (%)
Arecibo	9.28E+10	114.66	2.74	0.00	0.00	0.00
Low-resolution	6.23E+10	112.00	2.25	32.85	2.32	18.05
High-resolution	6.16E+10	114.00	2.23	33.59	0.58	18.51

<sup>a</sup> at 12 UTC

Noon <sup>b</sup>	$N_m E$	$h_m E$	$f_o E$	$\Delta_{rel}(N_m E)$	$\Delta_{rel}(h_m E)$	$\Delta_{rel}(f_o E)$
Arecibo	1.53E+11	108.34	3.53	0.00	0.00	0.00
Low-resolution	1.26E+11	105.00	3.20	17.81	3.08	9.34
High-resolution	1.33E+11	108.00	3.28	13.62	0.31	7.06

<sup>b</sup> at 16 UTC

Afternoon <sup>c</sup>	$N_m E$	$h_m E$	$f_o E$	$\Delta_{rel}(N_m E)$	$\Delta_{rel}(h_m E)$	$\Delta_{rel}(f_o E)$
Arecibo	1.21E+11	106.54	3.14	0.00	0.00	0.00
Low-resolution	1.14E+11	106.00	3.03	6.40	0.51	3.25
High-resolution	1.164E+11	107.00	3.07	4.06	0.43	2.05

<sup>c</sup> at 19 UTC

## 293 **4.2 Comparison between AURIC and COSMIC-1 GPS RO**

294 More than 850 individual ionospheric data profiles have been observed on February 9, 2012  
 295 by five of the six different COSMIC-1 micro satellites (one satellite (C003) was inactive during  
 296 the whole day). On this day, satellite-1 (C001) mapped Earth's ionosphere 287 times on its or-  
 297 bital path between 00:41-23:57 UTC. Satellite-2 (C002) produced 179 profiles between 04:12-  
 298 23:57 UTC. Satellite-4 (C004) observed 201 profiles from 00:07-23:55 UTC, satellite-5 (C005)  
 299 observed 66 profiles from 00:26-23:46 UTC, and Satellite-6 (C006) observed 162 profiles from  
 300 00:01-23:40 UTC. All these observations correspond to different latitudes and longitudes.

301 We impose three constraints to select appropriate ionospheric EDPs for comparison between  
 302 COSMIC-1 observations and AURIC model results. Criteria are listed below:

- 303 1. The time of the observed ionospheric data profile must coincide with daytime profiles (lo-  
 304 cal solar time morning, noon, and/or afternoon).
- 305 2. We choose only those occultation profiles which have latitude coverage within  $\pm 20^\circ$  and  
 306 longitude coverage within  $\pm 30^\circ$  of Arecibo and Millstone Hills to understand the latitu-  
 307 dinal effect of radio occultations. Also, lower atmosphere (below E-region) and upper at-  
 308 mosphere (F-1 region and above) condition would be similar for a single observation and  
 309 seasonal effect on ionospheric EDPs would be same.
- 310 3. No negative electron density above 100 km, and the altitude range of the observations must  
 311 not have a data gap within E-region altitudes ( $\sim 90 - 150$  km).

312 Our analysis of COSMIC-1 is limited from 100 km to 150 km. Below 100 km, we found  
 313 that some of the profiles carry negative electron density values. These misleading values may oc-  
 314 cur in the electron density profiles due to standard Abel inversion of the satellite radio signal (more  
 315 detail of this technique can be found in the work by Hajj & Romans, 1998, and references there  
 316 in) that assumes spherical symmetry (vertical electron density gradient only). Validation and er-  
 317 ror analysis of radio occultation data can be found in Schreiner et al. (1999). These negative val-  
 318 ues are the indication of the limitations of the profile retrievals if horizontal gradients are not con-  
 319 sidered in the inversion of occultation data (Lei et al., 2007). Mentioned earlier in section 2.1.3,  
 320 Pedatella et al. (2015) also found that standard Abel inversion ion profiles produce larger errors  
 321 in the E-region electron density measurements and proposed an improved inversion of electron

322 density profiles called gradient assisted ionospheric profiles ('igaPrf'). Up to date, UCAR had  
 323 recently (Nov, 2022) published 'igaPrf' profiles and became publicly available. Additionally, COSMIC-  
 324 1 observations do not coincide well during the chosen periods with Arecibo ISR and Millstone  
 325 Hills ISR. As COSMIC-1 observations show the sparseness of data availability, it is impracti-  
 326 cal to compare these COSMIC-1 profiles with radar observations rather we can run our model  
 327 in exact location of radio occultation profiles.

328 Figure 4 shows two radio occultation EDPs observed by COSMIC-1 in two different lat-  
 329 itude (low and middle, respectively), longitude, and local solar time. Our comparison is consis-  
 330 tent with the proposed hypothesis that the high-resolution cross section and solar irradiance pro-  
 331 duce more ionization at the E-region regardless the location or time. Specifically, left panel of  
 332 Figure 4 shows the curve from COSMIC-1 (C001) orbit at 16.15 UT (9.80 Hr local solar time).  
 333 Besides, we included another profile from COSMIC-1 (C005) (right panel of Figure 4) orbit at  
 334 12.22 UT (9.13 Hr local solar time). Our model setup is different for these two runs and updated  
 335 high-resolution runs by AURIC are more aligned with data, as well as, producing more ioniza-  
 336 tion than the low resolution runs.

### 337 4.3 Comparison between AURIC and empirical models

338 Two empirical models, IRI-2016 and FIRI-2018, are compared with AURIC model results  
 339 at the location of Arecibo ISR observations, as can be seen in Figure 5. The IRI-2016 model (web-  
 340 based version) incorporates several user required input parameters (see Table 2). Figure 5 presents  
 341 the IRI-2016 predicted EDP as a function of altitude between 90–150 km (dark green pentagon)  
 342 with a 1 km step size over-plotted with the hourly averaged EDP from the Arecibo campaign at  
 343 16 UTC. All other input parameters of IRI-2016 are set as default.

344 FIRI-2018, an improved version of IRI for the lower ionosphere (Friedrich et al., 2018),  
 345 is also included in that Figure 5. Here, we show the FIRI-2018 EDPs as a function of altitude (lime  
 346 green star) from 90–150 km. We also tabulated all the input parameters required for this em-  
 347 pirical model in Table 2.

348 A quantitative comparison in terms of  $N_mE$ ,  $h_mE$  and  $f_oE$  between the empirical mod-  
 349 els and AURIC is shown in Table 3. The IRI-2016 predicted EDP demonstrates differences of  
 350  $\sim 13.39\%$ ,  $\sim 0.28\%$  and  $\sim 6.93\%$  in terms of peak electron density, peak height, and critical  
 351 frequency ( $N_mE$ ,  $h_mE$ , and  $f_oE$ ) with the high-resolution AURIC run, respectively, while the  
 352 low-resolution model outputs show larger discrepancies. FIRI-2018 EDP shows small discrep-

**COSMIC-1 and AURIC  
electron density profiles comparison - 02/09/2012**

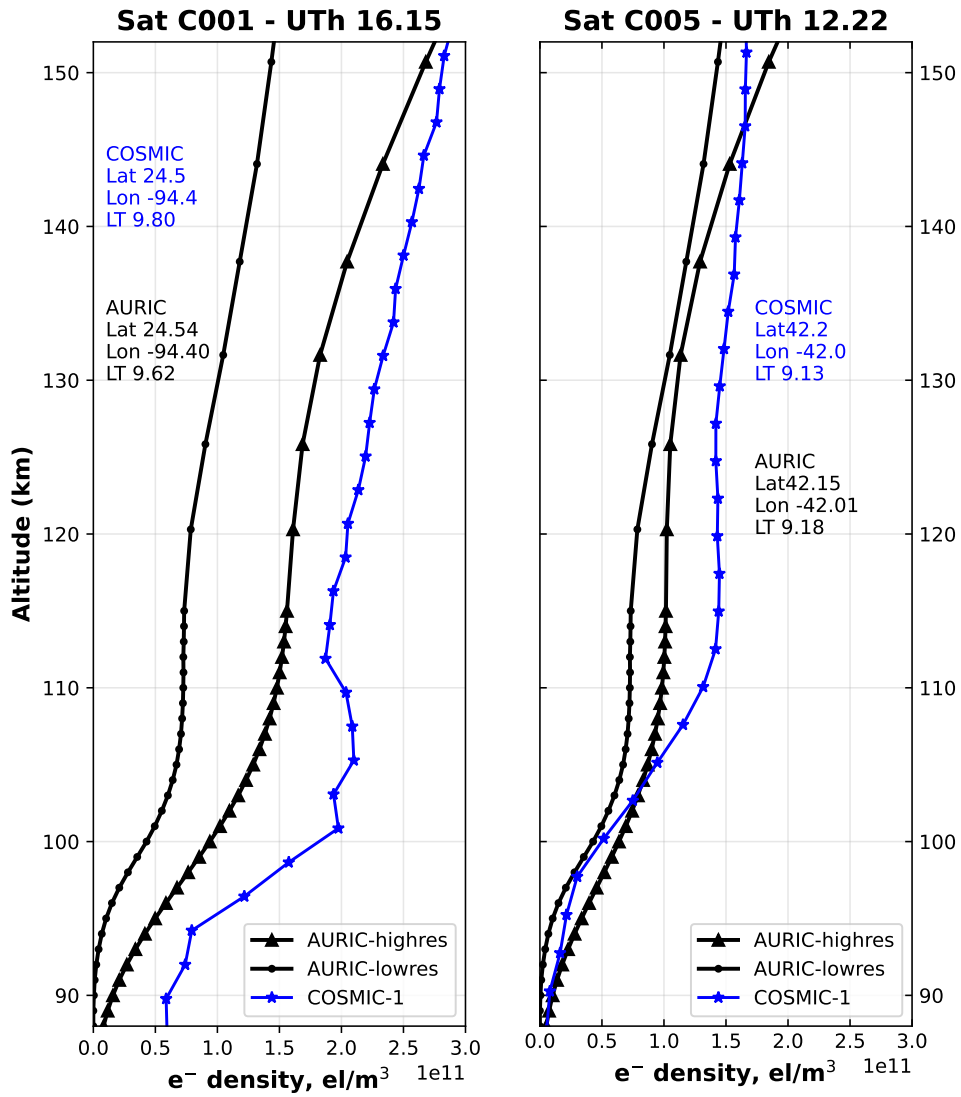


**Figure 4.** Comparison between observations by COSMIC-1 GPS RO profiles (blue star - iga profiles) with updated AURIC (black triangle - high-res, black circle - low-res) at the same location of radio occultations.

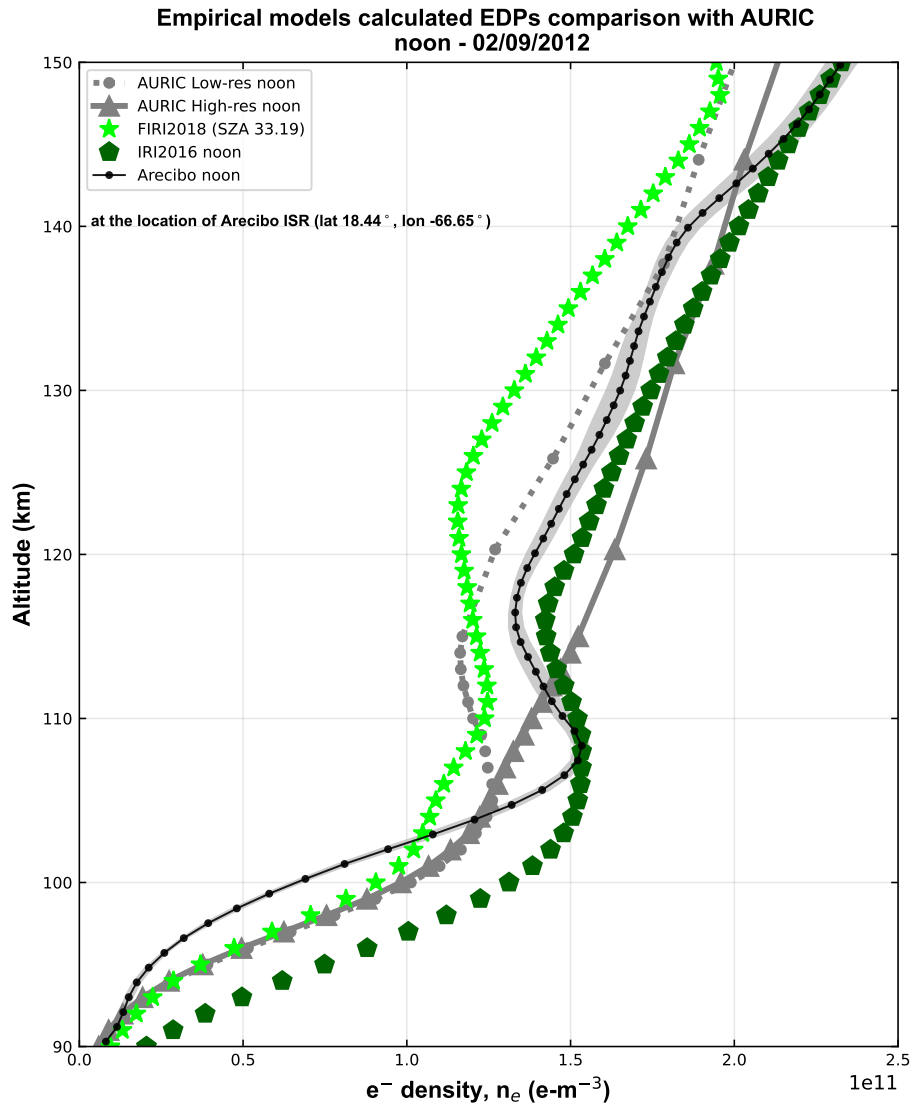


**Figure 5.** Comparison between empirical models (IRI-2016 (lime - triangle) and FIRI-2018 (sky blue - star)) with AURIC calculations (same as in Figure 4). Arecibo ISR observation (black circular solid line with shaded region as  $1\text{-}\sigma$  standard deviation) at the noon time is also presented as a reference.

**Table 2.** Selected input parameters of empirical models

	IRI-2016	FIRI-2018
Date	February 9, 2012	40 (J. Day)
Time (UTh)	16	33.19 (SZA)
Latitude (degree)	18.44° N	18.34° N
Longitude (degree)	293.4°	-
Altitude (km)	90-180	90-150
Stepsize (km)	1	1
Sunspot number	66.9	-
F10.7 radio flux (daily) (s.f.u.)	99.2	-
F10.7 radio flux (81-day) (s.f.u.)	115.1	-
Ionospheric index (IG12)	78.2	-

J = Julian; SZA = Solar Zenith Angle

353 ancy with the high-resolution model outputs in terms of  $N_m E$  and  $f_o E$  ( $\sim 6.01\%$  and  $\sim 3.35\%$ ,  
 354 respectively). The low-resolution model is more consistent with FIRI-2018 having less discrep-  
 355 ancy than the high-resolution model. Perhaps the better agreement with low-resolution AURIC  
 356 output is because FIRI-2018 also uses low-resolution cross sections (0.02 nm) of O<sub>2</sub> for Lyman-  
 357  $\alpha$  (Carver et al., 1977) reported by Friedrich and Torkar (2001).

#### 358 **4.4 Comparison between AURIC and Millstone Hills (MLH) ISR**

359 The Millstone Hills ISR data set contains three hours of electron density vertical profiles  
 360 during afternoon time only (18-19 Hr, 19-20 Hr, 20-21 Hr UTC) from just above  $\sim 95$  km to  
 361  $\sim 1000$  km. The left panel of Figure 6 shows individual 12 profiles of MLH alternating code  
 362 (AC) data between 18-19 Hr UTC (slate blue color) with  $\sim 4$  min cadence and altitudes rang-  
 363 ing from  $\sim 96$  km up to  $\sim 150$  km. The corresponding mean profile with observational uncer-  
 364 tainty (standard deviation) at 18-19 UTC is also shown in Figure 6 (dark navy blue with shaded  
 365 region as error). This plot demonstrates a peak electron density with values of  $1.264 \times 10^{11} m^{-3}$   
 366 at a height of 110.2 km. Similarly, the right panel of this Figure 6 demonstrates 15 profiles recorded  
 367 in one hour later i.e., 19-20 Hr UTC (light red) with the corresponding mean and standard de-  
 368 viation of the profiles shown as a brown diamond dotted line with shaded region as uncertainty.

369

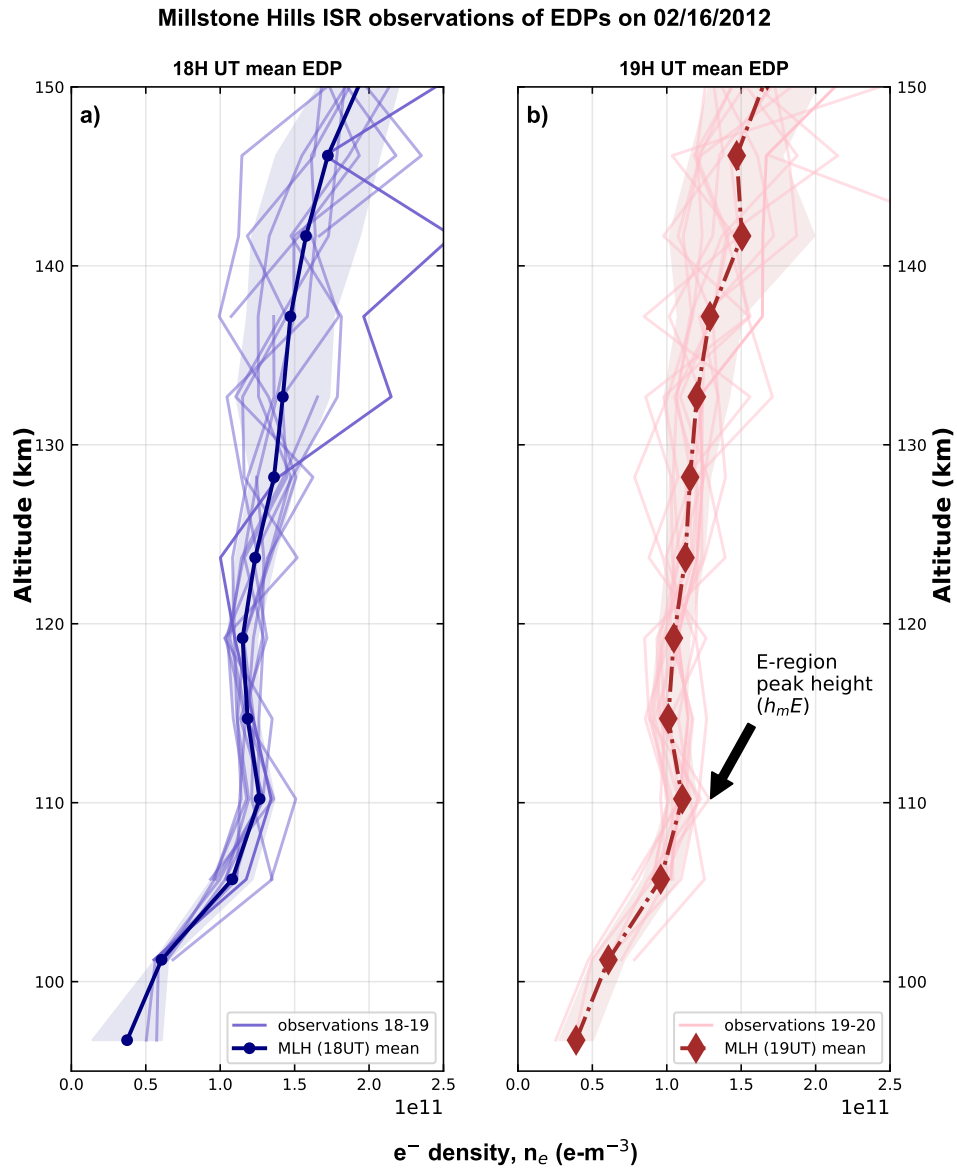


**Figure 6.** Millstone Hills ISR (42.61°N, 288.5°E) electron density observation with associated uncertainty as a function of altitude at 18 UTC (left panel) and 19 UTC (right panel) on February 16, 2012.

**Table 3.** Quantitative Comparison between empirical models and AURIC

Noon <sup>e</sup>	$N_m E$ ( $e^-/m^3$ )	$h_m E$ ( $km$ )	$f_o E$ ( $MHz$ )	$\Delta_{rel}(N_m E)$ (%)	$\Delta_{rel}(h_m E)$ (%)	$\Delta_{rel}(f_o E)$ (%)
IRI-2016	1.53E+11	108.30	3.52	0.00	0.00	0.00
Low-resolution	see Table 1 <sup>b</sup>	see Table 1 <sup>b</sup>	see Table 1 <sup>b</sup>	17.58	3.05	9.21
High-resolution	”	”	”	13.39	0.28	6.93

<sup>e</sup> at 16 UTC

Noon <sup>f</sup>	$N_m E$ ( $e^-/m^3$ )	$h_m E$ ( $km$ )	$f_o E$ ( $MHz$ )	$\Delta_{rel}(N_m E)$ (%)	$\Delta_{rel}(h_m E)$ (%)	$\Delta_{rel}(f_o E)$ (%)
FIRI-2018	1.25E+11	111.00	3.17	0.00	0.00	0.00
Low-resolution	see Table 1 <sup>b</sup>	see Table 1 <sup>b</sup>	see Table 1 <sup>b</sup>	0.88	5.41	0.82
High-resolution	”	”	”	6.01	2.70	3.35

<sup>f</sup> SZA = 33.19°**Table 4.** Quantitative Comparison between MLH ISR and AURIC

Afternoon <sup>g</sup>	$N_m E$ ( $e^-/m^3$ )	$h_m E$ ( $km$ )	$f_o E$ ( $MHz$ )	$\Delta_{rel}(N_m E)$ (%)	$\Delta_{rel}(h_m E)$ (%)	$\Delta_{rel}(f_o E)$ (%)
MLH	1.10E+11	110.21	2.99	0.00	0.00	0.00
Low-resolution	9.37E+10	108.00	2.76	15.13	2.01	7.88
High-resolution	9.51E+10	110	2.78	13.89	0.19	7.20

<sup>g</sup> at 19 UTC

370 While the E-region peak height ( $h_m E$ ) remains unchanged (110.2 km), the  $N_m E$  has slightly  
371 decreased ( $1.105 \times 10^{11} m^{-3}$ ) in comparison to profiles from the previous hour. This is expected  
372 as the Sun moves closer to the horizon and thus the solar radiation decreases. We compare the  
373 mean 19 Hr peak electron density value, peak height and calculated peak critical frequency with  
374 AURIC model results in Table 4. Figure 7 shows comparison of 19 UTC Millstone Hills ISR EDPs  
375 (brown diamonds dotted line) with AURIC. It is evident that AURIC prediction with high-resolution  
376 input at 19 Hr almost coincides with observation in between  $\sim 115$  km to  $\sim 135$  km. Clearly,  
377 the new AURIC calculation with high-resolution cross section inputs generates more realistic out-  
378 put than the low-resolution AURIC calculation.

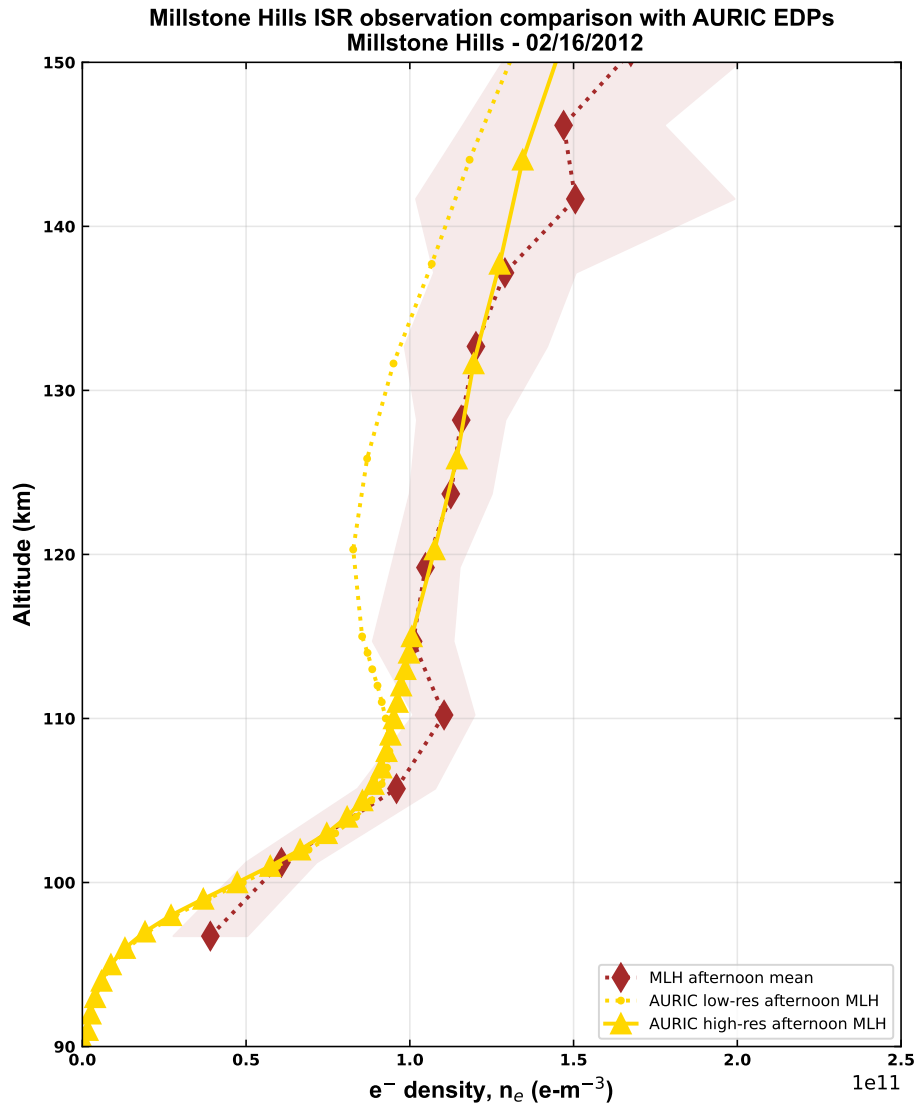


**Figure 7.** Comparison between Millstone Hills ISR observations (brown diamond dotted line) at 19 UTC with corresponding AURIC runs using the low-resolution (circular dotted) and the high-resolution (triangle solid) cross sections on February 16, 2012.

379 Relative percent difference between MLH ISR and AURIC model is in better agreement  
 380 in terms of  $N_m E$  and  $f_o E$  when we use the high-resolution cross section (13.89% and 7.20%,  
 381 discrepancy, respectively) than the low-resolution cross section as AURIC input (15.13% and 7.88%,  
 382 respectively). Peak height of E-region EDP in the low-resolution AURIC run is close to the ob-  
 383 servation ( $\sim 2\%$ ).

## 384 5 Discussion

385 As the photon flux from the Sun to the atmosphere varies with altitude, local time, loca-  
 386 tion and season, so do the EDPs in the E-layer (E. Appleton & Lyon, 1961; E. Appleton, 1963;  
 387 Chu et al., 2009), and  $N_m E$  varies accordingly. Both solar and magnetic activity strongly influ-  
 388 ence the magnitude and variability of electron densities at all ionospheric altitudes. The geomag-  
 389 netic and solar indices and radiative effects for the whole month of February 2012 are shown in  
 390 Figure 1. Planetary Kp index is lower ( $\sim 2$ ) for both days and the derived daily average of the  
 391 Ap index is also lower for February 9 and 16, (5 and  $\sim 4$ , respectively). These suggest that mag-  
 392 netic activity does not affect the EDP variations to a significant degree on our observational days.  
 393 Similarly, the F10.7 radio flux values of  $\sim 99$  and  $\sim 103$  s.f.u for those days are also an indi-  
 394 cation of relatively quiet solar activity. The number of sunspots are relatively small (28 and 48)  
 395 and there are no indications of any Earth directed coronal mass ejection or large class (X, M) so-  
 396 lar flare eruptions from the Sun on those observational days measured by two other important  
 397 ionospheric and thermospheric indices, which characterize the space weather and near-Earth space  
 398 environmental conditions are the Dst (Disturbance storm-time) index and soft x-rays (SXR) ob-  
 399 servation ( $\lambda \sim 1-8\text{\AA}$ ). We used these two indices for the month of February 2012 in addition to  
 400  $K_p$ ,  $A_p$ ,  $F_{10.7}$  and number of sunspots. Detailed study of solar soft x-rays including background,  
 401 origin, long term variability, and periodicity of SXR can be found in (Aschwanden, 1994). Data  
 402 source for GOES X-ray is NOAA Space Weather Prediction Center (SWPC) and we have uti-  
 403 lized GOES-15 level 2 X-ray sensor 1-minute irradiance average. The hourly equatorial Dst in-  
 404 dex is taken from the World Data Center for Geomagnetism, Kyoto, Japan. In February 2012,  
 405 the mean Dst index was mostly between 0 to -25 nT except on 15th February, 2012 when it was  
 406  $\sim -55$  nT (see Figure 1 panel (f)). Thus, the geomagnetic conditions were overall quiescent dur-  
 407 ing the observed period. In Figure 1 panel (e), we included the X-ray observation (longer wave-  
 408 length channel) by GOES satellite where it is clearly seen that X-ray flux always stays below  $10^{-5}$   
 409  $\text{W/m}^2$  except on 6th, 7th, and 11th February, 2012. In those days, the flux values are slightly above  
 410  $10^{-5} \text{W/m}^2$  which indicates an M-class flare activity. But, during our observation time, C-class

411 flare activity had been observed (i.e., 9th and 16th February, 2012, the x-ray flux is just above  
412  $10^{-6}$  W/m<sup>2</sup> and just below  $10^{-6}$  W/m<sup>2</sup>, respectively.) Overall, solar and geomagnetic conditions  
413 during the days of observation were relatively low and both days have similar solar and geomag-  
414 netic conditions.

415 In any ionospheric radiative transfer model, such as AURIC, three inputs should be con-  
416 sidered to calculate accurate results. These are : (1) Solar X ray and EUV irradiance (XUV all  
417 together) input, (2) Cross sections (photoabsorption + photoionization), and (3) neutral compo-  
418 sition and density as a function of altitude. In this paper, we selected two specific days (Febru-  
419 ary 9 and 16, 2012) when space weather was calm.

420 In AURIC, we can vary the solar irradiance input as per the space weather condition. For  
421 example, during high solar flare activity, the solar irradiance would be higher, which would al-  
422 low more XUV flux into the upper atmosphere and therefore, produce more ionization than the  
423 quiet time. So, theoretically, we should get more appropriate results from AURIC if we can set  
424 the correct EUV and X-ray irradiance to the model along with other inputs during high solar ac-  
425 tivity. But this paper is only evaluating the contribution of high-resolution cross sections keep-  
426 ing the solar irradiance fixed, and that is the reason we choose those two specific days when the  
427 sun is relatively quieter than the active time. Overall, by setting the correct solar irradiance and  
428 high-resolution cross sections in AURIC, in principal, we can generate the correct EDP profiles  
429 from AURIC even if it is not solar minimum condition.

430 Bulk of ionospheric measurement is too slow to gain any insight about quick changes in  
431 ionosphere (Meier et al., 2002). In order to test the model output in terms of electron density ver-  
432 tical profiles after employing certain updates such as high resolution photoionization and pho-  
433 toabsorption cross sections of two important atmospheric constituent N<sub>2</sub> and O, as well as, high-  
434 resolution solar spectrum (see Soto et al., 2023, for more detail), we simply use a single day anal-  
435 ysis to understand the E-region variability in daily manner. Sojka et al. (2014) studied Arecibo  
436 region E-layer with Arecibo ISR data campaign on February 9, 2012 and two of ionospheric mod-  
437 els incorporated high-resolution solar irradiance by Solar Dynamic Observatory (SDO) onboard  
438 Extreme Ultraviolet Variability Experiment (EVE). Our study utilize the same dateset. Figure  
439 2 shows the daily variability of electron density peak absolute value and height at E-region in a  
440 single day Arecibo ISR observation exactly same like Sojka et al. (2014). Uncertainty analysis  
441 and data variation can also be found in Sojka et al. (2014). On the other hand, Millstone hills ISR  
442 is located in different latitude and EDP measured on February 16, 2012. To compare with AU-  
443 RIC model data, we measured the hourly mean values from all ISR observations to keep local

444 time fixed and measured  $1-\sigma$  standard deviation at each altitude step to predict the measurement  
445 error. AURIC simulations presented in paper for Arecibo and Millstone comparison are in two  
446 different latitudes and two entirely different model setup.

447 AURIC predicts less ionization than data during early-morning regardless of the cross sec-  
448 tion inputs to the model (blue and cyan profiles in Figure 3). During noon (black and grey pro-  
449 files) and afternoon (red and majenta profiles in Figure 3), the model calculations show similar  
450 trends from  $\sim 90$  km to  $\sim 105$  km. Clearly, new high-resolution cross section calculations with  
451 a new high-resolution solar spectrum model produces a higher rate of photoionization, which is  
452 more distinctive above  $\sim 105$  km to  $\sim 110$  km. This specific altitude range is important, as the  
453 E-region peak electron density is usually located in this range. The peak at the E-region is not  
454 clearly detected in the new high resolution AURIC calculations. Therefore, we compare the model  
455 electron density value using the altitude of the real time  $h_m E$  observed by Arecibo ISR.

456 Two empirical models have been used in the study to compare with AURIC outputs. Gen-  
457 erally, Thermosphere and Ionosphere models are of two kinds, first, physics based models, such  
458 as AURIC, GLOW, and various general circulation models, etc., and the second kind is empirical/semi-  
459 empirical models such as IRI, FIRI. IRI-2016 is an empirical model which does not use any ex-  
460 isting theoretical approach for understanding ionospheric processes rather it is using real-time  
461 data from ground and space-based observations such as rocket sondes, radars, and more recently  
462 satellites. On the other hand, FIRI-2018 is a semi-empirical model, which is a combination of  
463 data and an ion-chemical model, specifically, using an analytical function for the lower ionosphere  
464 and neutral atmosphere and output is adjusted by a limited number of rocket measurements. Friedrich  
465 et al. (2018) mentioned two important limitations in the FIRI-2018 model. First, the use of ob-  
466 solete solar flux measurements (Delaboudinière et al., 1978; Manson, 1976), and, second, absorp-  
467 tion and ionization cross sections used in the model pose insufficient or lower resolution. There-  
468 fore, FIRI is very good for D-region electron density analysis, but perhaps, not precise for E-region  
469 EDP calculation as solar X-rays and EUV absorbs in E-region and it is required to have both high-  
470 resolution calculation and observations. Due to the differences in the underlying assumptions,  
471 mathematical formulations, and the amount of data assimilated, a certain degree of difference is  
472 natural among the different models. Especially, the theoretical models and empirical models are  
473 naturally very different, however, they empirical models are thought to capture the average (or  
474 typical) behavior of the atmosphere-ionosphere, therefore they are commonly used to validate  
475 theoretical models. In our comparison, it is evident that AURIC with  $N_2$  and O high resolution

476 cross sections and high-resolution solar irradiance profile is much better aligned with IRI-2016  
477 and the Arecibo radar profiles, which is a major improvement in a physics-based model.

478 Figures 3,4,5, and 7 confirm our hypothesis that high resolution absorption and ionization  
479 cross sections allow the penetration of much more solar EUV radiation into the E and D regions  
480 than is allowed by low-resolution cross sections (at a fixed location and time, the high -resolution  
481 cross section AURIC produces  $\sim 10\%$  more electrons than the low resolution run at 110 km,  
482 while at 120 km, the discrepancy rises to  $\sim 22\%$ ). However, electron densities computed from  
483 the high-resolution transmission do not agree in shape with the observations. There are several  
484 possible reasons for this discrepancy.

485 The photoionization rate around 120 km is controlled principally by two factors: the pas-  
486 sage of light through  $N_2$  and  $O_2$  molecular bands longward of 80 nm and the  $O_2$  photoioniza-  
487 tion cross section (Soto et al., 2023). The  $O_2$  bands are broadened in this region by predissoci-  
488 ation and can be spectrally resolved and measured accurately in the laboratory, so we do not con-  
489 sider them a source of uncertainty. On the other hand,  $N_2$  bands consist of a very large number  
490 of rotational lines that are not resolvable in the laboratory, so they must be modeled. Even with  
491 our model resolution of 0.001 nm, the spectral resolution is insufficient to reproduce the rotational  
492 line shapes, so the atmospheric transmission will only capture some of the peaks and valleys be-  
493 tween the rotational lines. Although this has a direct effect on the photoionization rate of  $O_2$  at  
494 120 km, our preliminary calculations indicate that any error resulting from 0.001 nm resolution  
495 is very small (less than 0.5%). A major redesign of AURIC is not within the scope of this work,  
496 though we hope to investigate this effect in the future.

497 Currently we compute the  $O_2$  photoionization rate using the cross section from the Conway  
498 (1988) compilation, which is traceable to the laboratory measurements of Samson et al. (1977,  
499 1982). Their measurements are not sufficient to resolve autoionization lines that play a signif-  
500 icant role in the penetration of solar EUV radiation to the lower ionosphere (Meier et al., 2007;  
501 Soto et al., 2023). It is possible that new theoretical calculations of the  $O_2$  cross section will im-  
502 prove the agreement between the models and observations in Figures 3,4,5, and 7. Finally, the  
503 AURIC model does not include diffusion or dynamics, which have the potential to alter the al-  
504 titude profiles. Investigation of these effects will be addressed in a future analysis.

505 Besides, Figure 8 shows a contribution plot of AURIC volume production rates (VPRs) as  
506 a function of altitude for February 9, 2012 at noon for four different flavours of AURIC. Volume  
507 production rates for the dominant three states of O,  $N_2$ , and  $O_2$  and a pseudo state for O (con-

508 taining the VPR contribution for 29 states) are shown as color-coded symbols (see legend) along  
509 with corresponding model EDP (dashed black line) and Arecibo observatory ISR EDP with mea-  
510 surement uncertainty (purple line). The total VPR are the orange circles. Panel (A) shows the  
511 AURIC model calculations utilizing the new high-resolution (0.001 nm) O and N<sub>2</sub> photoioniza-  
512 tion and photoabsorption cross sections and Conway (1988) O<sub>2</sub> cross section interpolated onto  
513 the high-resolution grid. Panel (B) illustrates the model results using the new cross sections binned  
514 onto a low-resolution grid (0.05 nm resolution from 0.1-10 nm and 0.1 nm resolution from 10-  
515 105 nm) and the Conway (1988) O<sub>2</sub> cross section on the low-resolution grid. Panel (C) shows  
516 the model results utilizing the Conway (1988) cross section compilation interpolated onto a high-  
517 resolution (0.001 nm) grid and panel (D) illustrates model results using the Conway (1988) com-  
518 pilation cross sections on the low-resolution grid. In the paper, “high-resolution” AURIC run cor-  
519 responds panel (A) and “low-resolution” AURIC run corresponds panel (D).

520       Indeed, the shape and magnitude of the O<sub>2</sub><sup>+</sup>(X) is the main contributor at lower altitude.  
521 However, in Panel A (new high resolution model results) we see increased O<sup>+</sup>(4So) VPR ex-  
522 tending down to about 110 km which is different from the other cases.

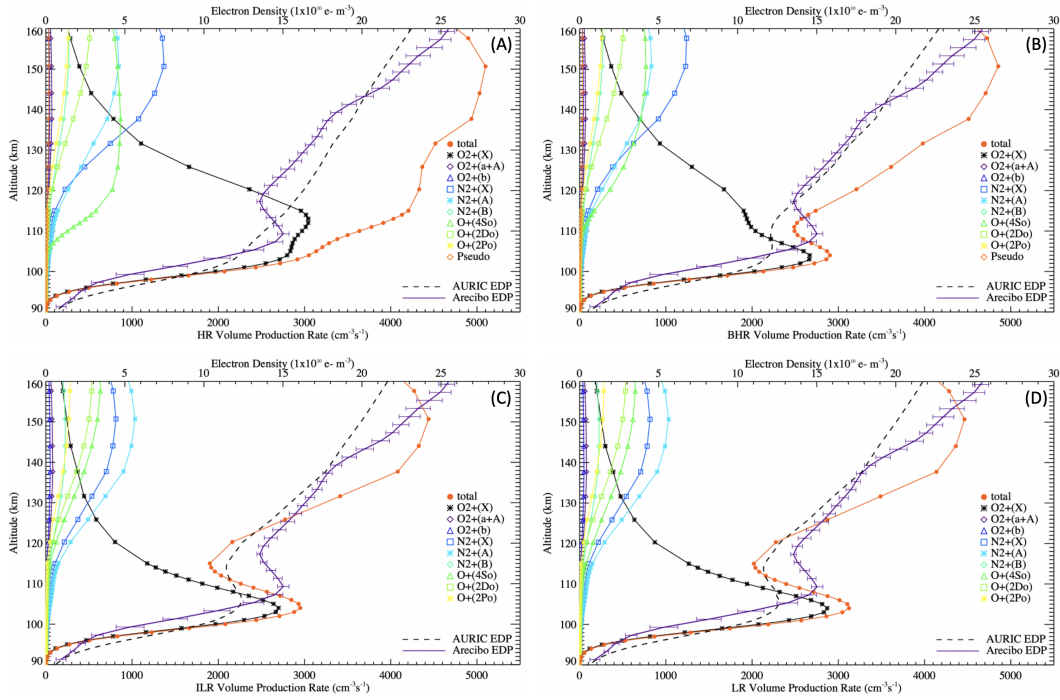


**Figure 8.** AURIC volume production rates vs altitude for February 9, 2012 16UTC (noon) are shown with the corresponding AURIC model EDP (dashed black line) and Arcibo Observatory ISR EDP with 1-sigma uncertainties (purple line).

## 6 Summary and Conclusion

AURIC calculations of varying flavors (i.e., different sets of photoionization and photoabsorption cross sections and solar EUV spectrum) are used to calculate the ion composition that leads to the calculation of electron density in the E-region. This study presents a summary of daily ionospheric electron number density observations by several methods, including two incoherent scatter radars, one satellite system, and two empirical models for a solar quiet day. We compare measured electron densities with the output of AURIC using two different inputs: high-resolution cross sections and solar spectral irradiance; and low-resolution cross sections. The main focus of this study is to take the first step and compare the real time EDPs with the output of a simplified model of the E-region using new calculations of high resolution cross sections and solar spectral irradiance.

It is evident that modeled E-region electron densities are significantly increased with the high resolution cross sections and are likely to account for the mismatch between earlier models and the data. Incorporating high-resolution cross section calculations in the AURIC model clearly increases the photoionization rate and therefore the electron density in the E-region, improving agreement with observations by radars, satellites, and empirical model calculations. However, the altitude profiles of the high resolution model EDPs do not generally agree with the data in terms of peak density. Future investigation of this work should address the inclusion of molecular oxygen ( $O_2$ ) high-resolution calculation of photoabsorption and photoionization cross sections in the model that may improve the agreement between observed and modeled E-region electron density profile shapes. Nevertheless, inter comparison between AURIC and other ionosphere models could well identify differences in physics, such as dynamics that could account for the mismatch with the data. Overall, considering all the uncertainties involved in calculation and data analysis discussed above, during a solar quiet day the simulated high-resolution version of AURIC and measured electron density vertical profiles are more aligned than the low-resolution AURIC runs.

## 549 **Appendix A : Physics of photoionization**

550 Absorption of photons at a certain wavelength (i.e., short wavelength; high frequency) by  
 551 a neutral atom causes the ejection of an electron, therefore, ions-electrons pairs form at the up-  
 552 per atmosphere of the Earth. It's called photoionization. E-region ionization occurs primarily by  
 553 solar extreme ultraviolet photons (EUV) and X-rays at certain energy ranges when  $\lambda$  (wavelength)  
 554  $< 100$  nm. Following Meier et al. (2007), The photoionization rate ( $j$ ) can be defined as the prod-  
 555 uct of ionization frequency ( $g$ ) and number density ( $n$ ) of the species ( $i$ ). Mathematically,

$$556 \quad j_i(z) = g_i(z) * n_i(z) \quad (\text{A1})$$

557 Unit of photoionization rate ( $j$ ) is ionization  $cm^{-3}s^{-1}$  if ionization frequency ( $g$ ) can be  
 558 expressed as unit of  $s^{-1}$  and number density ( $n$ ) is expressed as a unit of  $cm^{-3}$ . The ionization  
 559 frequency ( $g$ ) at high spectral resolution can be expressed as,

$$560 \quad g_i(z) = \int_0^{\lambda_i^t} \sigma_i(\lambda) F_s(\lambda) e^{-\tau(z,\lambda)} d\lambda \quad (\text{A2})$$

561 where,  $\sigma$  is the threshold wavelength photoionization cross section of the species ( $i$ ),  $F_s$  is the  
 562 solar spectral irradiance (unit: photons  $cm^{-2}s^{-1}nm^{-1}$ ) and  $\tau$  is the optical depth (or optical thick-  
 563 ness) at wavelength between the reference altitude altitude ( $z$ ) and the Sun.

564 The optical depth ( $\tau$ ) can be defined as (Yiğit, 2018)

$$565 \quad \tau(z, \lambda) = \sum_i \sigma_i^a(\lambda) \int_z^\infty n_i(z') ds, \quad (\text{A3})$$

566 where  $a$  stands for total absorption and  $s$  is the distance along the path of the penetrating pho-  
 567 tons. For an overhead Sun, solar zenith angle must be  $0^\circ$  which satisfies  $s = z'$ . The compu-  
 568 tation of ionization frequency is mostly carried out by mapping of cross sections and optical depths  
 569 for species O, O<sub>2</sub>, and N<sub>2</sub> respectively.

## 570 **Appendix B : E-region critical frequency**

571 Generally, an electromagnetic (EM) radio wave propagating from the ground to the iono-  
 572 sphere can be reflected by ionospheric layers, depending on the electron density profile. EM waves  
 573 with a higher frequency will penetrate and propagate to relatively higher altitudes. The maximum  
 574 frequency that can be reflected from the E-region layer (i.e., from  $\sim 90$  km up to  $\sim 150$  km)  
 575 is called the E-region critical frequency ( $f_oE$ ) which is proportional to the maximum electron  
 576 density in the E-region ( $N_mE$ ). The corresponding height of the peak E-region electron density

577 is denoted by  $h_m E$ . Photoelectrons are those that are at much higher than thermal energies, typ-  
 578 ically around 1-100 eV, produced in the E-region oscillate in response to the time varying elec-  
 579 tric field and can be described by the plasma frequency of electrons ( $\omega_{pe}$ ). Following equation  
 580 2.6 from Schunk and Nagy (2009) or equation 8(a) from Unz (1963) modified for Thomson scat-  
 581 ter radar observation (Evans, 1969; Semeter, 2020), we can express the critical frequency that  
 582 refers to the location at which maximum refraction occurs, and the height where we find the max-  
 583 imum electron density, in functional form:

$$584 \quad f_o E = \frac{1}{2\pi} \sqrt{\left( \frac{n_e * e^2}{\epsilon_0 * m_e} \right)} \approx 8.98 \sqrt{n_e} \approx 9 \sqrt{n_e}, \quad (\text{B1})$$

585 where,  $n_e = N_m E$  is the maximum electron density at the height of  $h_m E$ ,  $\epsilon_0$  is the permittiv-  
 586 ity at free space,  $e$  is the electron charge and  $m_e$  is the mass of electron. All parameters must be  
 587 expressed in SI units to evaluate Equation B1. Typically, for a summer day at low solar activity,  
 588 this value can range from 2–4 MHz and reach up to 6 MHz during high solar activity (Figure  
 589 1, Sheiner et al., 2020).

590 **Acronyms**

591 **AURIC** Atmospheric Ultraviolet Radiance Integrated Code

592 **COSMIC** Constellation observing system for meteorology ionosphere and climate

593 **COSPER** Committee on Space Research

594 **C/NOFS-CINDI** Communications/Navigation Outage Forecasting System - Coupled Ion-Neutral  
595 Dynamics Investigation

596 **EDP** Electron density profile

597 **GLOW model** GLobal AirglOW model

598 **ISR** Incoherent scatter radar

599 **IRI** International Reference Ionosphere

600 **MLH** Millstone Hills

601 **RO** Radio occultation

602 **SDO-EVE** Solar Dynamics Observatory - Extreme Ultraviolet Variability Experiment

603 **UCAR** University Corporation for Atmospheric Research

604 **URSI** International Union of Radio Science

605 **Acknowledgments**

606 The Arecibo Observatory is the principal facility of the National Astronomy and Ionosphere  
607 Center, which is operated by Cornell University under a cooperative agreement with the National  
608 Science Foundation (NSF). We appreciate Millstone Hills radar observatory and COSMIC-1 team  
609 for making their data publicly available. We also want to thank IRI and FIRI model development  
610 team for making their model available online. Additionally, we thank two reviewers for helpful  
611 comments and suggestions. This material is based upon work supported by the National Science  
612 Foundation under Grant No. 1849014.

613 **Data availability statement**

614 AURIC model outputs, Observational data from Arecibo ISR, COSMIC-1, IRI-2016, FIRI-  
615 2108, Millstone Hills ISR, and associated code needed to read the data files are publicly avail-  
616 able on Zenodo (Sakib et al., 2023).

617 **References**

- 618 Anderson, D., Forbes, J., & Codrescu, M. (1989). A fully analytic, low-and middle-latitude  
619 ionospheric model. *Journal of Geophysical Research: Space Physics*, *94*(A2), 1520–  
620 1524.
- 621 Anthes, R. A., Bernhardt, P., Chen, Y., Cucurull, L., Dymond, K., Ector, D., . . . others  
622 (2008). The cosmic/formosat-3 mission: Early results. *Bulletin of the American  
623 Meteorological Society*, *89*(3), 313–334.
- 624 Appleton, E. (1963). A seasonal anomaly in the ionospheric e-layer. *Journal of Atmospheric  
625 and Terrestrial Physics*, *25*(10), 577–579.
- 626 Appleton, E., & Lyon, A. (1961). Studies of the e-layer of the ionosphere—ii: Electro-  
627 magnetic perturbations and other anomalies. *Journal of Atmospheric and Terrestrial  
628 Physics*, *21*(2-3), 73–99.
- 629 Appleton, E. V., & Barnett, M. A. F. (1925). Local reflection of wireless waves from the up-  
630 per atmosphere. *Nature*, *115*(2888), 333–334.
- 631 Aschwanden, M. J. (1994). Irradiance observations of the 1–8 Å solar soft x-ray flux from  
632 goes. *Solar Physics*, *152*, 53–59.
- 633 Bailey, S. M., Barth, C. A., & Solomon, S. C. (2002). A model of nitric oxide in the lower  
634 thermosphere. *Journal of Geophysical Research: Space Physics*, *107*(A8), SIA–22.
- 635 Bartels, J. (1949). The standardized index, ks, and the planetary index, kp. *IATME Bull*,  
636 *97*(12b), 0001.
- 637 Bartels, J. (1957). The geomagnetic measures for the time-variations of solar corpuscular  
638 radiation, described for use in correlation studies in other geophysical fields. *Ann. In-  
639 tern. Geophys.*, *4*, 227–236.
- 640 Bell, K., & Stafford, R. (1992). Photoionization cross-sections for atomic oxygen. *Planetary  
641 and space science*, *40*(10), 1419–1424.
- 642 Berk, A., Bernstein, L. S., & Robertson, D. C. (1987). *Modtran: A moderate resolution  
643 model for lowtran* (Tech. Rep.). Spectral Sciences Inc Burlington MA.
- 644 Bilitza, D., Altadill, D., Truhlik, V., Shubin, V., Galkin, I., Reinisch, B., & Huang, X. (2017).  
645 International reference ionosphere 2016: From ionospheric climate to real-time  
646 weather predictions. *Space weather*, *15*(2), 418–429.
- 647 Bilitza, D., Pezzopane, M., Truhlik, V., Altadill, D., Reinisch, B. W., & Pignalberi, A.  
648 (2022). The international reference ionosphere model: A review and description  
649 of an ionospheric benchmark. *Reviews of Geophysics*, e2022RG000792.

- 650 Bilitza, D., Rawer, K., Bossy, L., & Gulyaeva, T. (1993). International reference iono-  
 651 sphere—past, present, and future: I. electron density. *Advances in Space Research*,  
 652 *13*(3), 3–13.
- 653 Brown, S., Bilitza, D., & Yiğit, E. (2018). Ionosonde-based indices for improved representa-  
 654 tion of solar cycle variation in the international reference ionosphere model. *Journal of*  
 655 *Atmospheric and Solar-Terrestrial Physics*, *171*, 137–146.
- 656 Carver, J. H., Gies, H., Hobbs, T., Lewis, B., & McCoy, D. (1977). Temperature dependence  
 657 of the molecular oxygen photoabsorption cross section near the h lyman  $\alpha$  line. *Jour-*  
 658 *nal of Geophysical Research*, *82*(13), 1955–1960.
- 659 Chu, Y.-H., Wu, K.-H., & Su, C.-L. (2009). A new aspect of ionospheric e region electron  
 660 density morphology. *Journal of Geophysical Research: Space Physics*, *114*(A12).
- 661 Clette, F., & Lefèvre, L. (2016). The new sunspot number: assembling all corrections. *Solar*  
 662 *Physics*, *291*(9), 2629–2651.
- 663 Conway, R. R. (1988). *Photoabsorption and photoionization cross sections of o, o2, and n2*  
 664 *for photoelectron production calculations: A compilation of recent laboratory mea-*  
 665 *surements.* (Tech. Rep.). NAVAL RESEARCH LAB WASHINGTON DC. Retrieved  
 666 from <https://apps.dtic.mil/sti/pdfs/ADA193866.pdf>
- 667 Delaboudinière, J.-P., Donnelly, R., Hinteregger, H., Schidtke, G., & Simon, P. (1978). *In-*  
 668 *tercomparison/compilation of relevant solar flux data related to aeronomy (solar cycle*  
 669 *20); cospar technique manual 7.*
- 670 Evans, J. V. (1969). Theory and practice of ionosphere study by thomson scatter radar. *Pro-*  
 671 *ceedings of the IEEE*, *57*(4), 496–530.
- 672 Friedrich, M., Pock, C., & Torkar, K. (2018). Firi-2018, an updated empirical model of  
 673 the lower ionosphere. *Journal of Geophysical Research: Space Physics*, *123*(8), 6737–  
 674 6751.
- 675 Friedrich, M., & Torkar, K. (2001). Firi: A semiempirical model of the lower ionosphere.  
 676 *Journal of Geophysical Research: Space Physics*, *106*(A10), 21409–21418.
- 677 Gustafsson, G., Papitashvili, N., & Papitashvili, V. (1992). A revised corrected geomag-  
 678 netic coordinate system for epochs 1985 and 1990. *Journal of atmospheric and terres-*  
 679 *trial physics*, *54*(11-12), 1609–1631.
- 680 Hajj, G. A., & Romans, L. J. (1998). Ionospheric electron density profiles obtained with the  
 681 global positioning system: Results from the gps/met experiment. *Radio Science*, *33*(1),  
 682 175–190.

- 683 Hedin, A. E. (1991). Extension of the msis thermosphere model into the middle and lower  
684 atmosphere. *Journal of Geophysical Research: Space Physics*, *96*(A2), 1159–1172.
- 685 Hinteregger, H. E., Fukui, K., & Gilson, B. R. (1981). Observational, reference and model  
686 data on solar evf, from measurements on ae-e. *Geophysical Research Letters*, *8*(11),  
687 1147–1150.
- 688 Lai, P.-C., Burke, W. J., & Gentile, L. (2013). Topside electron density profiles observed at  
689 low latitudes by cosmic and compared with in situ ion densities measured by c/nofs.  
690 *Journal of Geophysical Research: Space Physics*, *118*(5), 2670–2680.
- 691 Lean, J., Woods, T., Eparvier, F., Meier, R., Strickland, D., Correira, J., & Evans, J. (2011).  
692 Solar extreme ultraviolet irradiance: Present, past, and future. *Journal of Geophysical  
693 Research: Space Physics*, *116*(A1).
- 694 Lean, J. L., Coddington, O., Marchenko, S. V., Machol, J., DeLand, M. T., & Kopp, G.  
695 (2020, August). Solar Irradiance Variability: Modeling the Measurements. *Earth and  
696 Space Science*, *7*, 00645. doi: 10.1029/2019EA000645
- 697 Lean, J. L., Warren, H. P., Mariska, J. T., & Bishop, J. (2003, February). A new model of so-  
698 lar EUV irradiance variability 2. Comparisons with empirical models and observations  
699 and implications for space weather. *Journal of Geophysical Research (Space Physics)*,  
700 *108*(A2), 1059. doi: 10.1029/2001JA009238
- 701 Lei, J., Liu, L., Wan, W., & Zhang, S.-R. (2005). Variations of electron density based on  
702 long-term incoherent scatter radar and ionosonde measurements over millstone hill.  
703 *Radio science*, *40*(2), 1–10.
- 704 Lei, J., Syndergaard, S., Burns, A. G., Solomon, S. C., Wang, W., Zeng, Z., . . . others  
705 (2007). Comparison of cosmic ionospheric measurements with ground-based obser-  
706 vations and model predictions: Preliminary results. *Journal of Geophysical Research:  
707 Space Physics*, *112*(A7).
- 708 Link, R., Strickland, D. J., & Daniell Jr, R. (1993). Auric airglow modules: Phase 1 develop-  
709 ment and application. In *Ultraviolet technology iv* (Vol. 1764, pp. 132–141).
- 710 Majeed, T., & Strickland, D. J. (1997). New survey of electron impact cross sections for  
711 photoelectron and auroral electron energy loss calculations. *Journal of Physical and  
712 Chemical Reference Data*, *26*(2), 335–349.
- 713 Manson, J. E. (1976). The solar extreme ultraviolet between 30 and 205 Å on november 9,  
714 1971, compared with previous measurements in this spectral region. *Journal of Geo-  
715 physical Research*, *81*(10), 1629–1635.

- 716 Matzka, J., Stolle, C., Yamazaki, Y., Bronkalla, O., & Morschhauser, A. (2021). The geo-  
717 magnetic kp index and derived indices of geomagnetic activity. *Space Weather*, *19*(5),  
718 e2020SW002641.
- 719 McGranaghan, R., Knipp, D. J., Solomon, S. C., & Fang, X. (2015). A fast, parameterized  
720 model of upper atmospheric ionization rates, chemistry, and conductivity. *Journal of*  
721 *Geophysical Research: Space Physics*, *120*(6), 4936–4949.
- 722 Meier, R., McLaughlin, B. M., Warren, H., & Bishop, J. (2007). Atomic oxygen photoion-  
723 ization rates computed with high resolution cross sections and solar fluxes. *Geophysi-*  
724 *cal research letters*, *34*(1).
- 725 Meier, R., Warren, H., Nicholas, A., Bishop, J., Huba, J., Drob, D., . . . others (2002).  
726 Ionospheric and dayglow responses to the radiative phase of the bastille day flare.  
727 *Geophysical research letters*, *29*(10), 99–1.
- 728 Pedatella, N., Yue, X., & Schreiner, W. (2015). An improved inversion for formsat-  
729 3/cosmic ionosphere electron density profiles. *Journal of Geophysical Research:*  
730 *Space Physics*, *120*(10), 8942–8953.
- 731 Prölss, G. (2012). *Physics of the earth's space environment: an introduction*. Springer Sci-  
732 ence & Business Media.
- 733 Rawer, K., Bilitza, D., & Ramakrishnan, S. (1978). Goals and status of the international ref-  
734 erence ionosphere. *Reviews of geophysics*, *16*(2), 177–181.
- 735 Sakib, M. N., Soto, E., Yigit, E., Evans, J. S., & Meier, R. R. (2023, February). *Vali-*  
736 *validation of E-region Model Electron Density Profiles using High-Resolution Cross*  
737 *Sections*. Zenodo [Dataset]. Retrieved from [https://doi.org/10.5281/](https://doi.org/10.5281/zenodo.8117507)  
738 [zenodo.8117507](https://doi.org/10.5281/zenodo.8117507) doi: 10.5281/zenodo.8117507
- 739 Samson, J. A., Gardner, J., & Haddad, G. (1977). Total and partial photoionization cross-  
740 sections of o2 from 100 to 800 Å. *Journal of Electron Spectroscopy and Related Phe-*  
741 *nomena*, *12*(3), 281–292.
- 742 Samson, J. A., Rayborn, G. H., & Pareek, P. (1982). Dissociative photoionization cross  
743 sections of o2 from threshold to 120 Å. *The Journal of Chemical Physics*, *76*(1), 393–  
744 397.
- 745 Schreiner, W. S., Sokolovskiy, S. V., Rocken, C., & Hunt, D. C. (1999). Analysis and vali-  
746 dation of gps/met radio occultation data in the ionosphere. *Radio Science*, *34*(4), 949–  
747 966.
- 748 Schunk, R., & Nagy, A. (2009). *Ionospheres: physics, plasma physics, and chemistry*. Cam-

- 749 bridge university press.
- 750 Semeter, J. (2020). High-resolution approaches to ionospheric exploration. In *The dynamical*  
751 *ionosphere* (pp. 223–241). Elsevier.
- 752 Sharma, R., Brown, J., Berk, A., Acharya, P., & Gruninger, J. (1996). *User’s manual*  
753 *for samm, sharc and modtran merged*. (Tech. Rep.). SPECTRAL SCIENCES INC  
754 BURLINGTON MA.
- 755 Sheiner, O., Rakhlin, A., Fridman, V., & Vybornov, F. (2020). New ionospheric index for  
756 space weather services. *Advances in Space Research*, *66*(6), 1415–1426.
- 757 Sheng, C., Deng, Y., Yue, X., & Huang, Y. (2014). Height-integrated pedersen conductivity  
758 in both e and f regions from cosmic observations. *Journal of Atmospheric and Solar-*  
759 *Terrestrial Physics*, *115*, 79–86.
- 760 Shiokawa, K., & Georgieva, K. (2021). A review of the scostep’s 5-year scientific program  
761 varsi—variability of the sun and its terrestrial impact. *Progress in Earth and Plane-*  
762 *tary Science*, *8*(1), 1–43.
- 763 Sojka, J. J., Jensen, J. B., David, M., Schunk, R. W., Woods, T., Eparvier, F., . . . Eccles, J. V.  
764 (2014). Ionospheric model-observation comparisons: E layer at arecibo incorporation  
765 of sdo-eve solar irradiances. *Journal of Geophysical Research: Space Physics*, *119*(5),  
766 3844–3856.
- 767 Solomon, S. C. (2006). Numerical models of the e-region ionosphere. *Advances in Space*  
768 *Research*, *37*(5), 1031–1037.
- 769 Solomon, S. C., Hays, P. B., & Abreu, V. J. (1988). The auroral 6300 Å emission: Observa-  
770 tions and modeling. *Journal of Geophysical Research: Space Physics*, *93*(A9), 9867–  
771 9882.
- 772 Soto, E., Evans, J., Meier, R. R., Tashiro, M., Sakib, M. N., & Yiğit, E. (2023). A miss-  
773 ing piece of the e-region puzzle: The need for high-resolution photoionization cross  
774 sections and solar irradiance in models. *JGR: Space Physics*. (Submitted)
- 775 Strickland, D., Bishop, J., Evans, J., Majeed, T., Shen, P., Cox, R., . . . Huffman, R. (1999).  
776 Atmospheric ultraviolet radiance integrated code (auric): Theory, software architec-  
777 ture, inputs, and selected results. *Journal of Quantitative Spectroscopy and Radiative*  
778 *Transfer*, *62*(6), 689–742.
- 779 Strickland, D. J., Evans, J. S., Bishop, J. E., Majeed, T., Shen, P. M., Link, R., & Huffman,  
780 R. E. (1996). Atmospheric ultraviolet radiance integrated code (auric): Current ca-  
781 pabilities for rapidly modeling dayglow from the far uv to the near ir. In *Ultraviolet*

- 782           *atmospheric and space remote sensing: Methods and instrumentation* (Vol. 2831, pp.  
783           184–199).
- 784 Tapping, K. (2013). The 10.7 cm solar radio flux (f10.7). *Space weather*, 11(7), 394–406.
- 785 Unz, H. (1963). The magneto-ionic theory for bound electrons. *Journal of Atmospheric and*  
786           *Terrestrial Physics*, 25(5), 281–286.
- 787 Ward, W., Seppälä, A., Yiğit, E., Nakamura, T., Stolle, C., Laštovička, J., . . . Pallamraju,  
788           D. (2021). Role Of the Sun and the Middle atmosphere/thermosphere/ionosphere  
789           In Climate (ROSMIC): a retrospective and prospective view. *Progress in Earth and*  
790           *Planetary Sciences*, 8(1), 47. doi: 10.1186/s40645-021-00433-8
- 791 Warren, H. P. (2005). A solar minimum irradiance spectrum for wavelengths below 1200 Å.  
792           *The Astrophysical Journal Supplement Series*, 157(1), 147.
- 793 Woods, T. N., Eparvier, F. G., Hock, R., Jones, A. R., Woodraska, D., Judge, D., . . . Viereck,  
794           R. (2012, January). Extreme Ultraviolet Variability Experiment (EVE) on the Solar  
795           Dynamics Observatory (SDO): Overview of Science Objectives, Instrument Design,  
796           Data Products, and Model Developments. *Solar Physics*, 275(1-2), 115-143. doi:  
797           10.1007/s11207-009-9487-6
- 798 Yan, R., Zhima, Z., Xiong, C., Shen, X., Huang, J., Guan, Y., . . . Liu, C. (2020). Comparison  
799           of electron density and temperature from the cses satellite with other space-borne and  
800           ground-based observations. *Journal of Geophysical Research: Space Physics*, 125(10),  
801           e2019JA027747.
- 802 Yiğit, E., & Medvedev, A. S. (2015). Internal wave coupling processes in earth's atmosphere.  
803           *Advances in Space Research*, 55(4), 983–1003.
- 804 Yiğit, E., Knížová, P. K., Georgieva, K., & Ward, W. (2016). A review of vertical coupling  
805           in the atmosphere-ionosphere system: Effects of waves, sudden stratospheric warm-  
806           ings, space weather, and of solar activity. *J. Atmos. Sol.-Terr. Phys.*, 141, 1–12. doi:  
807           http://dx.DOI.org/10.1016/j.jastp.2016.02.011
- 808 Yiğit, E. (2018). Planetary Ionospheres: Magnetic Fields, Chemical Processes, and Iono-  
809           spheric Structure. In *Atmospheric and Space Sciences: Ionospheres and Plasma Envi-*  
810           *ronments* (pp. 67–102). Cham: Springer International Publishing. Retrieved 2022-02-  
811           15, from [http://link.springer.com/10.1007/978-3-319-62006-0\\_4](http://link.springer.com/10.1007/978-3-319-62006-0_4)  
812           (Series Title: SpringerBriefs in Earth Sciences) doi: 10.1007/978-3-319-62006-0\_4
- 813 Zhang, S.-R., Holt, J. M., & Kurdzo, J. (2011). Millstone hill isr observations of upper at-  
814           mospheric long-term changes: Height dependency. *Journal of Geophysical Research:*

